

**Fault Tolerant Attitude Sensing and Force Feedback
Control for Unmanned Aerial Vehicles**

A Thesis

Submitted to the Faculty

of

Drexel University

by

Chirag Jagadish

in partial fulfillment of the

requirements for the degree

of

Doctor of Philosophy

June 2009



Office of Graduate Studies Dissertation/Thesis Approval Form

This form is for use by all doctoral and master's students with a dissertation/thesis requirement. Please print clearly as the library will bind a copy of this form with each copy of the dissertation/thesis. All doctoral dissertations must conform to university format requirements, which is the responsibility of the student and supervising professor. Students should obtain a copy of the Thesis Manual located on the library website.

Dissertation/Thesis Title: Fault Tolerant Attitude Sensing and
Force Feedback Control For Unmanned
Aerial Vehicles

Author: CHIRAG JAGADISH

This dissertation/thesis is hereby accepted and approved.

Signatures:

Examining Committee

Chair

Borchen Chang

Members

Christine M. Pelletier

Sori ST

Pradeep Kumar

P. N. N. N.

J. S.

Academic Advisor

Borchen Chang

Department Head

S. Kalidindi/Alau

© Copyright 2009

Chirag Jagadish. All Rights Reserved.

DEDICATIONS

To my parents.

ACKNOWLEDGMENTS

I would like to thank many people for their support and contribution towards my research through all these years. First and foremost is my academic advisor Dr. B. C. Chang, without whose help and unrelenting support this work would not be possible. I would also like to thank Dr. Sorin Siegler, Dr. Harry Kwatny and Dr. Pravat Nagvajara for all the help and wonderful classes. Many thanks to Dr. Ajmal Yousuff for giving me the opportunity to serve him as a teaching assistant. I would also like to thank Dr. Christine Belcastro for her invaluable and timely inputs. I also have to thank Dr. Alan Lau and Dr. Bradley Layton for their timely help. I take this opportunity to thank all my previous and present lab-mates – Dr. Chun-Long Hu, Elie Ballouz, Hui-Ping Cheng, Ketan Chemburkar, Ho-Lung Li and Mishah Salman for their tremendous support and co-operation. Last but not the least I would like to thank my parents for their unwavering support.

Table of Contents

Dedications	iv
List of Tables	ix
List of Figures	x
Abstract	xi
1. Introduction.....	14
1.1 Motivation	15
1.2 Literature survey.....	17
1.3 Contributions of the thesis.....	18
1.4 Organization of the thesis	20
2. Attitude Computation Background	22
2.1 Direction Cosine Matrix	22
2.2 Davenport's Q Method	24
2.3 The Euler Angle Method	26
3. Diversified Redundancy Through Multiple Euler Angle Computation Methods	31
3.1 The general rotation angle conversion algorithm	32
3.2 Rotation Sequences and Euler Angle Computation.....	33
3.2.1 Yaw-Pitch-Roll or Aerospace Rotation Sequence	33
3.2.2 Roll-Pitch-Yaw sequence (RPY)	33
3.2.3 Yaw-Roll-Pitch sequence (YRP)	35
3.2.4 Roll-Yaw-Pitch sequence (RYP)	36
3.2.5 Pitch-Roll-Yaw sequence (PRY)	37
3.2.6 Pitch-Yaw-Roll sequence (PYR)	38
3.2.7 Yaw-Pitch-Roll-2 (YPR_2)	39

3.2.8	Yaw-Pitch-Yaw sequence (YPY).....	40
3.2.9	Yaw-Roll-Yaw sequence (YRY)	41
3.2.10	Roll-Pitch-Roll sequence (RPR).....	41
3.2.11	Roll-Yaw-Roll sequence (RYR).....	42
3.2.12	Pitch-Roll-Pitch sequence (PRP)	43
3.2.13	Pitch-Yaw-Pitch sequence (PYP)	43
3.3	Fault Tolerance in Attitude Determination.....	44
3.4	Computational Issues.....	47
3.4.1	Singularity	47
3.4.2	Inverse Trigonometric Function Ambiguities / Quadrant Selection	49
4.	Euler Angle Computation of NASA GTM UAV on a Bank-to-Turn Maneuver.....	52
4.1	NASA GTM UAV System Dynamic Model and Controller Development	52
4.2	Euler Angle Computation with Disturbance Affected Accelerometer	57
5.	Joy-Stick Force Feedback System	65
5.1	Hardware description.....	65
5.2	Force Feedback Joy-Stick Dynamic Model.....	67
6.	Joy-Stick Force Feedback Controller Design	69
6.1	Joy-Stick Speed Regulator – Hybrid Controller.....	69
6.2	UAV stabilization and tracking controller.....	73
6.3	Overall Closed Loop System & Computer Simulation	73
7.	Conclusion	78

List of Tables

Table 1. Different computation methods and sensor axes used

Table 2. Effect of Singularity & sensor noise.

Table 3. Euler angles computed at time instant 0.3 sec.

Table 4. Euler angles computed at time instant 3 sec.

Table 5. Euler angles computed at time instant 10 sec.

List of Figures

- Figure 1 Reference frame XYZ with body fixed sensors \hat{u} , \hat{v} and \hat{w} .
- Figure 2. Relation between axes and their respective rotation angles.
- Figure 3. Reference position of vehicle & directions of sensors axes mounted on vehicle.
- Figure 4. UAV bank-to-turn maneuver.
- Figure 5. Generalized UAV plant and controller K in closed loop.
- Figure 6. Structure of multi-variable controller K .
- Figure 7. Accelerometer measurements from simulation.
- Figure 8. Simulated magnetic field measurement.
- Figure 9. Euler angle results from the PYR, RPR & RYR rotation sequences.
- Figure 10. Gravity components reconstructed from Euler angles.
- Figure 11. Inertial acceleration components ex , ey , ez .
- Figure 12. Prototype remote control joy-stick regulation system.
- Figure 13. Joy-Stick angular speed regulation through variable feedback gain hybrid controller.
- Figure 14. Master motor discrete hybrid controller switching strategy.
- Figure 15. Bode plot of DC motor with PI controller.
- Figure 16. Overall system with user applied torque being the main input and the slave motor angle being the main output of interest.
- Figure 17. User applied input torque to joy-stick.
- Figure 18. Reference roll angle applied by joy-stick angle and the UAV response.
- Figure 19. DC motor control input voltage.

Abstract

Fault Tolerant Attitude Sensing and Force Feedback
Control for Unmanned Aerial Vehicles

Chirag Jagadish

Advisor: B. C. Chang, PhD.

Two aspects of an unmanned aerial vehicle are studied in this work. One is fault tolerant attitude determination and the other is to provide force feedback to the joy-stick of the UAV so as to prevent faulty inputs from the pilot.

Determination of attitude plays an important role in control of aerial vehicles. One way of defining the attitude is through Euler angles. These angles can be determined based on the measurements of the projections of the gravity and earth magnetic fields on the three body axes of the vehicle. Attitude determination in unmanned aerial vehicles poses additional challenges due to limitations of space, payload, power and cost. Therefore it provides for almost no room for any bulky sensors or extra sensor hardware for backup and as such leaves no room for sensor fault issues either. In the face of these limitations, this study proposes a fault tolerant computing of Euler angles by utilizing multiple different computation methods, with each method utilizing a different subset of the available sensor measurement data. Twenty-five such methods have been presented in this document. The capability of computing the Euler angles in multiple ways provides a diversified redundancy required for fault tolerance. The proposed approach can identify certain sets of sensor failures and even separate the reference fields from the disturbances. A bank-to-turn maneuver of the NASA GTM UAV is used to demonstrate the fault tolerance provided by the proposed method as well as to demonstrate the method

of determining the correct Euler angles despite interferences by inertial acceleration disturbances.

Attitude computation is essential for stability. But as of today most UAVs are commanded remotely by human pilots. While basic stability control is entrusted to machine or the on-board automatic controller, overall guidance is usually with humans. It is therefore the pilot who sets the command/references through a joy-stick. While this is a good compromise between complete automation and complete human control, it still poses some unique challenges.

Pilots of manned aircraft are present inside the cockpit of the aircraft they fly and thus have a better feel of the flying environment and also the limitations of the flight. The same might not be true for UAV pilots stationed on the ground. A major handicap is that visual feedback is the only one available for the UAV pilot. An additional parameter like force feedback on the remote control joy-stick can help the UAV pilot to physically feel the limitation of the safe flight envelope. This can make the flying itself easier and safer. A method proposed here is to design a joy-stick assembly with an additional actuator. This actuator is controlled so as to generate a force feedback on the joy-stick. The control developed for this system is such that the actuator allows free movement for the pilot as long as the UAV is within the safe flight envelope. On the other hand, if it is outside this safe range, the actuator opposes the pilot's applied torque and prevents him/her from giving erroneous commands to the UAV.

1. INTRODUCTION

UAVs or unmanned aerial vehicles are increasingly being used in military as well as civilian applications. As with any other aerial vehicle, flight control of an unmanned aerial vehicle requires knowledge of its translational displacements (position), angular displacements (attitude) and their time derivatives. In particular angular displacements are closely related to the stability of the vehicle. Monitoring and controlling angular displacement or angular position to stay within a safe flight envelope is necessary in maintaining stability.

Angular position represented through angles called Euler angles can be computed using measurements of universally available fields like gravity and magnetic field of earth. Sensors like accelerometer and magnetometers are mounted on the vehicle for this purpose. But these sensors are prone to failures and at the same time any extraneous fields acting on them can throw the angle computations off. Sensor redundancy in the form of use of multiple sensors is limited due to restrictions of pay load, space, power requirement and cost of the UAV.

This work explores the possibility of providing redundancy and thereby fault-tolerance in Euler angle computation using different subsets within the available set of measurements. Each measurement subset is then utilized in the computation through a different angle computation method.

Accurate attitude information is essential in control of any aerial vehicle. A common way of controlling a UAV is to design a closed loop controller which maintains stability and tracks commands while the overall guidance or commands could be defined by the pilots. These commands could be reference signals like speed or attitude angles for the aircraft

defined through a joy-stick. The on-board controller could then track these reference signals. While pilots of manned aircraft get to experience the real flight conditions, remote pilots of UAVs lack this feel of the flying environment and depend purely on visual feedback. Any error in input through wrong movement of the joy-stick could lead to erroneous references being set for the UAV with disastrous consequences. In this study a controller is designed so as to develop a force feedback through an actuator attached to joy-stick so as to prevent erroneous joy-stick movements. This can reduce or prevent common mistakes due to pilot oversight.

1.1 Motivation

The angular displacements or attitude is represented in many different ways like direction cosine matrices, quaternion and Euler angles. The focus in this study is on Euler angles or roll, pitch, and yaw angles - ϕ , θ , and ψ . Euler angles are usually defined based on a particular rotation sequence called as aerospace or yaw-pitch-roll rotation sequence.

In order to compute these Euler angles, reference fields like gravity and magnetic field of earth are utilized. These fields are assumed given and are known constant over a span of time and space. Earth gravity and magnetic fields are measured through 3-axis MEMS (Micro Electro Mechanical Systems) accelerometer and a 3-axis AMR (Anisotropic Magneto Resistive) magnetometer respectively. These sensors measure the 3 mutually perpendicular projections of earth gravity and magnetic fields in the three dimensional space.

An equation to compute Euler angles based on the yaw-pitch-roll rotation sequence utilizes the three measurements: gravity measurement in x direction - g_x , gravity

measured in y direction - g_y and magnetic field measurement in x direction - m_x . If all these three measurements are accurate and reliable, then the other three measurements - m_y , m_z and g_z , become unnecessary. However, in real applications, sensors may fail and/or the measurements may be contaminated by extraneous fields. Contamination of even one of the three critical sensors could produce an erroneous angular position of the vehicle. Any control effort based on such an erroneous angular position could cause catastrophic results.

Sensor failure issues can be resolved by employing duplicate sensors but this cannot resolve issues caused by extraneous fields like inertial acceleration and disturbance magnetic field. This is due to the fact that an extraneous field would affect both the main sensor and all its duplicates in a similar fashion. Multiple types of sensors could be used and the data merged. But space, pay load, power and cost restrictions on the UAV make this method infeasible in most cases. It is these situations that the diversified redundancy method proposed in this work becomes effective and useful. In this method a minimal increase in hardware and an increase in computations produce a new kind of redundancy which can help solve problems arising due to fault on certain sets of sensors.

Accurate information of attitude is necessary but this information alone does not ensure a fail-safe control of the UAV. Even though stabilization is taken care of for the given flight condition, flying any aircraft still depends on the pilot's commands. The attempt here is to design a joy-stick controller to help the pilot in giving accurate commands.

A way of helping the pilot which is prevalent as of today is to give him/her as much information as possible. Presently this is done mainly through visual feedback. But this information becomes so much that the pilot is unable to handle this flood of information

effectively. This can lead to longer training periods as well as confusion even for trained pilots. This confusion can increase chances of a crash. Alternative methods of relaying information like tilting the UAV pilot's chair to track the attitude of the UAV or applying force feedback on the joy-stick to stop the pilot from giving erroneous or adventurous inputs are ways that could be explored to improve this man-machine interaction. The latter is studied in more detail in this work.

1.2 Literature survey

The computation of attitude of flying vehicles is important and has been extensively studied for decades [1]-[3]. Direction cosine matrix was among the oldest methods developed for three axis attitude parameterization [1], [3]-[6].

Fault tolerant sensing issues have been studied extensively too [7]. One proposed solution is to employ duplicate sensors [7], [8]. This overcomes the problems related to component failure but cannot resolve those caused by extraneous fields like inertial acceleration [9] and disturbance magnetic field. Use of multiple sensors of different types has also been proposed. The data from each type is later merged to obtain the attitude information [10]. More sensors can help, but as the UAV becomes smaller, the payload, space and power constraints may limit the use of multiple sensors. Kalman estimation [6], [10], [12] is one way to estimate the states of a system in cases related to sensor failures. In order to use this approach, the knowledge of the system dynamics model and the stochastic characteristics of the interferences and noises are required.

The approach proposed in this study utilizes different subsets of the available measurements through multiple computation methods [11], [13]. With a minimal to no increase in hardware and increased computation it is seen that the redundancy and fault

tolerance in the sensor system is increased. This redundancy which is contributed mainly by the multiple ways of computing will be addressed to as diversified redundancy in this document. A few more details of the proposed approach follow in the next subsection.

Remote control joy-sticks have been utilized in many different applications. UAVs have been the most visible ones. But the concept used in remote surgeries is basically similar to that of a joy-stick remote control. Force feedback for medical applications or haptics has been a topic of extensive study more recently [17], [18]. Video gaming industry is another one which has shown keen interest in joy-stick and of-late in the concept of force feedback [19]. Another important application for force feedback is in the joy-stick of a wheel chair. Here the user is assisted in avoiding obstacles through force feedback applied to the joy-stick [20], [21], [22].

The application demonstrated in this work is related to UAV. Here the force feedback is provided to the pilot's joy-stick such that he is disallowed from giving erroneous/adventurous inputs as reference commands to the UAV.

1.3 Contributions of the thesis

Euler angles can be computed in a fault tolerant manner by utilizing multiple alternative computation methods. These computations are such that each method uses a different rotation-sequence matrix and thereby requires a different subset of sensor data among the three accelerometer and three magnetometer measurements available. Despite using the different sets of data, all the computation methods are all utilized for the same purpose of computing Euler angles corresponding to the aerospace or YPR rotation angles. The ability to use different subsets of sensor measurements improves fault tolerance in the

sensor system. This creates a type of redundancy called diversified redundancy. Even simple algorithms like majority vote among the various angle computation results is seen to accomplish the task of distinguishing the right Euler angle from among all the available results. This improves the fault tolerance and reliability of the sensing system.

In addition to improving the fault tolerance, it is also seen that in some circumstances the proposed approach is also capable of computing the exact value of the extraneous field that had influenced the sensors. This allows for dead-reckoning in some special cases.

If the roll, pitch, and yaw rates are available and the flight dynamics of the UAV is known, observer and Kalman filter theory can be used to estimate the Euler angles. Additional information can help solve some numerical issues in the proposed method. In addition more sensors like solid state rate gyros can also be of help in contributing to the proposed redundancy and to cover for many more cases or combinations of sensor issues. Knowledge of accurate attitude angles helps the on-board stability controller to maintain stability of the aircraft. But it is the pilot who sets reference speeds and angles through the joy-stick. If an erroneous reference is set, the on-board controller still attempts to track it. This reference could be a linear speed which is too high or too low such that the aircraft is at risk of breaking apart or stalling. The reference could also be a pitch or roll angle which is so large that the UAV loses lift. Pilot oversight could be a possible reason for erroneous joy-stick inputs.

The method proposed here attempts to help the pilot by providing force feedback which opposes the joy-stick movement whenever the controller senses that the pilot is in error. Here the joy-stick still produces the references for the on-board controller but the joy-stick itself is controlled by an actuator and a controller in addition to the pilot applied

torque. If the UAV is within a safe flight envelope, the joy-stick actuator is disabled and the entire operation is left to the user. If the UAV's measurement parameters indicate that it is outside the safe flight envelope, the actuator is activated so as to resist the user torque input to the joy-stick. This helps restrict the joy-stick to within a region where the reference commands generated maintain the UAV in safe flight.

It is to be noted here that the definition of safe flight conditions vary with the state of the flight. As an example, when the UAV is taking off or landing, the range of safe flight roll angle could be as small as 2° while the same for cruise condition might be as large as 10° . So a mechanical stop on the joy-stick might not be a good solution if sufficient flexibility and performance is required.

1.4 Organization of the thesis

The rest of the thesis is organized as follows. In the following chapter, background material regarding Euler angles and rotation matrices is provided. Alternative approaches like Direction Cosine Matrix and the Q Method based on Quaternion are also briefly described; their unsuitability in providing effective diversified redundancy is explained. Chapter 3 explains the variety of different ways developed to compute the Euler angles based on various subsets of sensor measurements. This chapter also explains the algorithms developed to improve the reliability of the sensor system based on the multiple Euler angle computation methods. Some common numerical issues that plague the Euler angle method and solutions for those issues are also prescribed. In Chapter 4 a simulation of a bank-to-turn maneuver of NASA GTM UAV is used to demonstrate the ability of the proposed approach to accurately compute the Euler angles under the influence of acceleration due to its motion. It also demonstrates the method to compute

the values of the inertial acceleration of the UAV. The joy-stick force feedback mechanism is designed to limit erroneous commands from being given to the UAV. The joy-stick assembly is described and its dynamic model developed in Chapter 5. A hybrid controller is developed to achieve the goals. The overall closed loop system consisting of the controlled joy-stick assembly and the UAV is simulated and the results are presented in Chapter 6. Concluding remarks follow in Chapter 7.

2. ATTITUDE COMPUTATION BACKGROUND

The computation of the attitude of a flying vehicle is important and has been extensively studied for decades. The three main approaches for attitude determination are briefly reviewed in the following.

2.1 Direction Cosine Matrix

Among the earliest methods developed for attitude determination was the direction cosine matrix method. This method requires three independent, mutually orthogonal parameters which can be measured through suitable sensors fixed on the vehicle. This triad of sensors has 3 axes each, thus producing three 3-dimensional unit vectors \hat{u} , \hat{v} and \hat{w} . Each element in these vectors is the dot product or projection of the respective body unit vector on a reference axis (Figure 1). Any change in the orientation of the vehicle produces the measurement vectors $\hat{u} = [u_1 \ u_2 \ u_3]^T$, $\hat{v} = [v_1 \ v_2 \ v_3]^T$ and $\hat{w} = [w_1 \ w_2 \ w_3]^T$. Arranging these three vectors in the form of a 3×3 matrix, we obtain the direction cosine matrix A given in (1). This matrix uniquely describes the attitude of the vehicle.

$$A = \begin{bmatrix} u_1 & u_2 & u_3 \\ v_1 & v_2 & v_3 \\ w_1 & w_2 & w_3 \end{bmatrix} \quad (1)$$

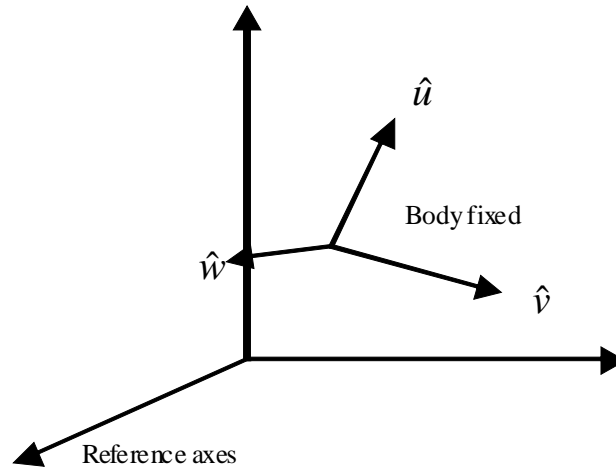


Figure 1 Reference frame XYZ with body fixed sensors \hat{u} \hat{v} and \hat{w}

The main advantage in direction cosine matrix method is its simplicity; it has no singularity problems and no inverse trigonometric computations involved. However the main drawback is that it requires three independent non-parallel parameters which can be measured using suitable sensors. But it is intuitively known that two vectors suffice in completely describing the attitude of the vehicle. Therefore we can say that the third set of measurements is redundant and is an extra burden on the sensor system. Another issue with this system is that even if a single sensor axis out of the nine measurements fail or is affected by an extraneous disturbance, the attitude represented would be erroneous. Having multiple types of sensors can resolve this problem but in the present method the combination of sensor information in providing the attitude is not optimal in any statistical sense.

An improvement to the direction cosine matrix method was the TRIAD method developed in 1964 by Harold D. Black [27]. TRIAD utilizes two measurement vectors instead of three. But solving for the attitude using this method is through an iterative

procedure. Moreover this method again does not accommodate for an optimal combination of multiple sensors data.

2.2 Davenport's Q Method

Attitude computation using the methods described in Section 2.1 would consume a lot of time on the computers of the 1960's and 70's. This did not allow for real time implementation of these algorithms. This led to the development of the Q method in 1977 by Paul Davenport [28].

The Q method was developed as one of the solutions for Wahba's problem [29]. In order to solve the Wahba's problem it is required to find the proper orthogonal matrix A in order to minimize the loss function in (2).

$$L(A) = \frac{1}{2} \sum_i a_i |b_i - Ar_i|^2 \quad (2)$$

b_i are the 3-dimensional vector measurements from the different sensor vectors, r_i are their respective initial unit vectors in the reference frame, a_i are the non-negative weights for each of the i measurements. The result of Wahba's problem is the A matrix which describes the orientation of the vehicle.

In order to solve Wahba's problem the A matrix is parameterized by a unit quaternion $Q_u = [q \ q_4]^T$. Here q describes the vector part while q_4 describes the scalar part of the quaternion. The optimal unit quaternion Q_{opt} which minimizes the Wahba's loss function is found to be the normalized eigenvector of K_e corresponding to the largest eigenvalue λ_{\max} . Here,

$$K_e Q_{opt} = \lambda_{\max} Q_{opt} \quad (3)$$

where, K_e is a symmetric traceless matrix.

$$K_e = \begin{bmatrix} S - I \operatorname{tr}(B) & z \\ z^T & \operatorname{tr}(B) \end{bmatrix} \quad (4)$$

Here B is the summation of products of the measured vectors b_i with transpose of their corresponding initial vectors r_i . S and z are defined as

$$S = B + B^T \quad \text{and} \quad z = \sum_i a_i b_i \times r_i$$

Then quaternion Q_{opt} describes the attitude of the vehicle. But even this method was not fast enough for the olden day computers. Improvements like QUEST method [30] was developed for the same purpose.

The Q method and later improvements like QUEST were developed in NASA mainly for use in spacecraft attitude determination. Spacecraft typically carry multiple types of sensors like sun sensors, star trackers, horizon sensors, magnetometers, etc. Q method allowed multiple sensor data to be combined efficiently along with individual weightings for each sensor. If one of elements in the sensor vector fails or is affected by an extraneous disturbance, the entire vector can be given a lesser weighting or can be discarded altogether. Provided that it is possible to carry multiple sensors on board, redundancy in the form of multiple sensors can be used to great advantage through this method. The combining of the multiple sensor data can be done optimally.

However, a partial failure of a sensor or an extraneous field affecting one of its three measurements would render the entire sensor vector un-usable. Other methods related to the Q method like the QUEST and SVD have similar drawbacks. Since a UAV has

constraints on pay load, space, cost and power, mounting too many sensors might not be feasible. Among the limited available sensor information, discarding an entire vector due to a single failure is a waste of valuable resources. In a constrained environment such as the one on a UAV it is essential to utilize every functional sensor.

2.3 The Euler Angle Method

This is the method which is of main interest in this work. Unlike the direction cosine and Q methods, the Euler angle method allows the freedom to choose individual entries of interest from the sensor measurement vectors and use them to compute the attitude. This provides unique advantages as will be discussed in later sections.

The principle involved in Euler angle method is that any angular position of the vehicle can be represented through a set of three successive rotations about the three mutually perpendicular axes. The three angles through which the vehicle undergoes rotations are called Euler angles. This set of three rotation angles and the sequence of axes completely describe the body's angular position.

Consider a rigid body with a body fixed sensor. At the reference position, this sensor measures the three mutually orthogonal projections of an independent space fixed vector and produces the measurement vector $\begin{bmatrix} x & y & z \end{bmatrix}^T$. This is called as the reference vector.

A yaw or a rotation from this position about the z axis through an angle ψ would produce the new sensor measurement vector $\begin{bmatrix} x' & y' & z' \end{bmatrix}^T$. The relation between this new vector and the reference vector can be described by (5).

$$\begin{bmatrix} x' \\ y' \\ z' \end{bmatrix} = \begin{bmatrix} \cos \psi & \sin \psi & 0 \\ -\sin \psi & \cos \psi & 0 \\ 0 & 0 & 1 \end{bmatrix} \begin{bmatrix} x \\ y \\ z \end{bmatrix} \quad (5)$$

Starting from this yaw rotated position, further rotations about the y axis through an angle θ followed by a rotation about x axis through ϕ produces vectors - $[x'' \ y'' \ z'']^T$ and $[u \ v \ w]^T$ respectively. The equations for the above rotations can be given as

$$\begin{bmatrix} x'' \\ y'' \\ z'' \end{bmatrix} = \begin{bmatrix} \cos \theta & 0 & -\sin \theta \\ 0 & 1 & 0 \\ \sin \theta & 0 & \cos \theta \end{bmatrix} \begin{bmatrix} x' \\ y' \\ z' \end{bmatrix} \quad (6)$$

and,

$$\begin{bmatrix} u \\ v \\ w \end{bmatrix} = \begin{bmatrix} 1 & 0 & 0 \\ 0 & \cos \phi & \sin \phi \\ 0 & -\sin \phi & \cos \phi \end{bmatrix} \begin{bmatrix} x'' \\ y'' \\ z'' \end{bmatrix} \quad (7)$$

Figure 2 shows the relation between the different rotation angles and their respective axes of rotation. The relation between the final measurement vector $[u \ v \ w]^T$ and the reference vector $[x \ y \ z]^T$ can be given through the equation shown in (8).

$$\begin{bmatrix} u \\ v \\ w \end{bmatrix} = \begin{bmatrix} c\theta c\psi & c\theta s\psi & -s\theta \\ s\phi s\theta c\psi - c\phi s\psi & s\phi s\theta s\psi + c\phi c\psi & s\phi c\theta \\ c\phi s\theta c\psi + s\phi s\psi & c\phi s\theta s\psi - s\phi c\psi & c\phi c\theta \end{bmatrix} \begin{bmatrix} x \\ y \\ z \end{bmatrix} \quad (8)$$

where, $c\theta$ represents $\cos \theta$, $s\phi$ is $\sin \phi$ etc. The final measurement vector is known through sensor measurements while the initial reference vector is known. This allows us to compute the three angles of rotation θ , ϕ and ψ through the equation in (8).

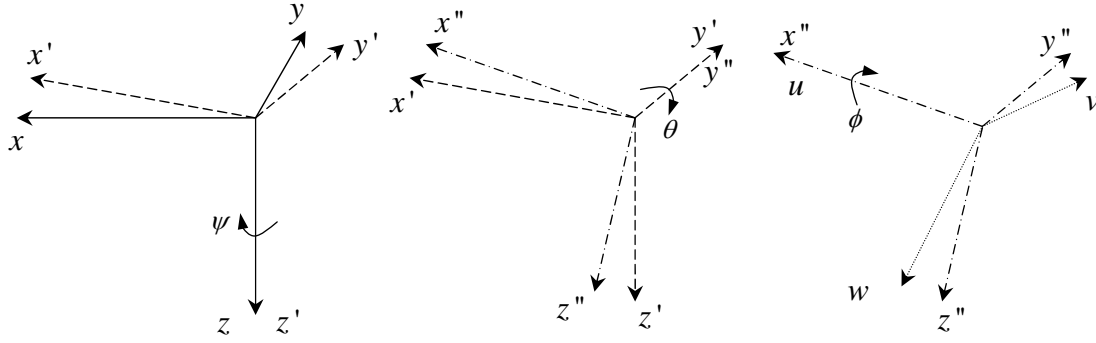


Figure 2. Relation between axes and their respective rotation angles.

Utilizing the Euler angle method in order to compute the attitude of the vehicle is possible when two non-parallel, space-fixed and measurable fields are available. Two such fields which are readily and universally available are earth gravity and earth magnetic field. Suitable sensors which can measure these fields are the 3-axis accelerometer and 3-axis magnetometer. Accelerometer measures the acceleration that the body is subjected to. Magnetometer measures the magnetic field that is incident on it. The axes of these sensors measure the projection of these fields in three mutually orthogonal directions. These fields being constant over a period of time and space provide constant references with respect to which the body's angular position can be measured and expressed.

Calculating Euler angles using rotation matrix method is simplified if the reference vectors of acceleration and magnetic field are considered to be in the form $[0 \ 0 \ 1]^T$ and $[\cos \alpha \ 0 \ \sin \alpha]^T$ respectively, where, α is the inclination angle of the earth magnetic field. In order to have the above mentioned reference vectors, initial reference position of the vehicle is considered to be such that its xz plane is vertical and coincides with the plane of the magnetic field [32] of earth and xy plane is horizontal and parallel

to the surface of the earth. The sensors are mounted on the body such that their axes are aligned with those of the body frame. Refer Figure 3.

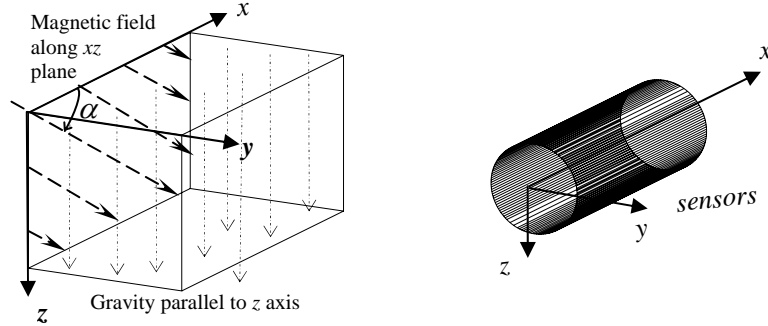


Figure 3. Reference position of vehicle & directions of sensors axes mounted on vehicle.

Once the vehicle undergoes a change in its angular position, sensor measurements at the accelerometer and magnetometer [9], [31] produce $\begin{bmatrix} g_x & g_y & g_z \end{bmatrix}^T$ and $\begin{bmatrix} m_x & m_y & m_z \end{bmatrix}^T$ respectively. Using these vectors and initial reference vectors $\begin{bmatrix} 0 & 0 & 1 \end{bmatrix}^T$ and $\begin{bmatrix} \cos \alpha & 0 & \sin \alpha \end{bmatrix}^T$ in equation (8), can help in computation of the three rotation angles or Euler angles. This is shown below.

$$\begin{aligned} \begin{bmatrix} g_x \\ g_y \\ g_z \end{bmatrix} &= \begin{bmatrix} c\theta c\psi & c\theta s\psi & -s\theta \\ s\phi s\theta c\psi - c\phi s\psi & s\phi s\theta s\psi + c\phi c\psi & s\phi c\theta \\ c\phi s\theta c\psi + s\phi s\psi & c\phi s\theta s\psi - s\phi c\psi & c\phi c\theta \end{bmatrix} \begin{bmatrix} 0 \\ 0 \\ 1 \end{bmatrix} \\ \begin{bmatrix} m_x \\ m_y \\ m_z \end{bmatrix} &= \begin{bmatrix} c\theta c\psi & c\theta s\psi & -s\theta \\ s\phi s\theta c\psi - c\phi s\psi & s\phi s\theta s\psi + c\phi c\psi & s\phi c\theta \\ c\phi s\theta c\psi + s\phi s\psi & c\phi s\theta s\psi - s\phi c\psi & c\phi c\theta \end{bmatrix} \begin{bmatrix} c\alpha \\ 0 \\ s\alpha \end{bmatrix} \end{aligned} \quad (9)$$

Using the equation in (9), the Euler angles can be computed as

$$\begin{aligned} \theta &= -\sin^{-1}(g_x) \\ \phi &= \sin^{-1}(g_y / \cos \theta) \\ \psi &= \cos^{-1}([m_x + \sin \theta \sin \alpha] / [\cos \theta \cos \alpha]) \end{aligned} \quad (10)$$

It can be seen from (10) that Euler angle computation using the Yaw-Pitch-Roll rotation sequence matrix relies on three of the six available measurements - g_x , g_y and m_x . The

disadvantages are that this method requires inverse trigonometric computations and this involves singularity problems. Inverse trigonometric computations also tend to be more time consuming when implemented on a computer or microprocessor. Despite these drawbacks, the Euler angle attitude computation method provides certain unique advantages. One of the most important advantages is that the attitude is determined through individual sensor measurements and not using entire vectors of measurements. This fact is exploited to develop a new type of redundancy which is referred to as diversified redundancy. The development of this redundancy and the advantages it provides is discussed in the following chapter.

3. DIVERSIFIED REDUNDANCY THROUGH MULTIPLE EULER ANGLE COMPUTATION

METHODS

In the previous section, representing the attitude of a vehicle using angles corresponding to the Yaw-Pitch-Roll (YPR) or the aerospace sequence of rotations was demonstrated. This sequence is among the more commonly used rotation sequences and the angles are referred to here as Euler angles. It was also seen that the YPR rotation Euler angle determination required the measurements - g_x , g_y and m_x . Similarly to this sequence, there are 11 other rotation sequences - RPY (Roll-Pitch-Yaw), YRP, RYP, PRY, PYR, YPY, YRY, RPR, RYR, PRP and PYP. Each of these rotation sequences have different direction cosine matrices and hence different inverse trigonometric functions are involved in the computation of the rotation angles. The subsets of sensor measurements involved in each computation method are also different. If all the different sequence angles can be converted to the corresponding YPR or aerospace sequence rotation angles, it would effectively allow the YPR Euler angles to be computed by utilizing different subsets of measurement data.

This ability to compute the Euler angles based on different subset of sensor data helps in creating a new type of redundancy called diversified redundancy. Using the twelve rotation sequences, at least twenty five different Euler angle computation methods can be developed. These methods are listed in Table 1 towards the end of this section. Almost all of them are seen to utilize different subsets of sensor data. Thirteen prominent ones among these and their related equations are explained in section 3.2. The general algorithm to convert any given rotation sequence angles to the YPR Euler angles is explained in the following.

3.1 The general rotation angle conversion algorithm

The general algorithm to convert a given set of rotation angles from one sequence to another is as follows.

Consider any reference vector $[i]^T = [i_x \ i_y \ i_z]^T$. Multiplying this vector with a rotation

matrix $[\alpha] = \begin{bmatrix} a_{11} & a_{12} & a_{13} \\ a_{21} & a_{22} & a_{23} \\ a_{31} & a_{32} & a_{33} \end{bmatrix}$ produces the final vector $[o]^T = [o_x \ o_y \ o_z]^T$. Since $[\alpha]$

is a rotation matrix $[\alpha][\alpha]^T = I$ where, I is unity matrix. Therefore

$$[o] = [\alpha][i] \quad (11)$$

$$[i] = [\alpha]^T [o] \quad (12)$$

The same output vector $[o]$ can be arrived at by multiplying the reference vector $[i]$ with

a different rotation matrix $[\beta] = \begin{bmatrix} b_{11} & b_{12} & b_{13} \\ b_{21} & b_{22} & b_{23} \\ b_{31} & b_{32} & b_{33} \end{bmatrix}$.

$$[o] = [\beta][i] \quad (13)$$

Substituting the expression for $[i]$ from (12) into (13), we get

$$\begin{aligned} [o] &= [\beta] [\alpha]^T [o] \\ \therefore [\beta] &= [\alpha] \end{aligned} \quad (14)$$

All the rotation matrices of the various rotation sequences discussed earlier have similar property to that shown in (14). This allows derivation of equations that can convert any given rotation sequence angle to the YPR angles. The section 3.2.2 demonstrates this concept.

3.2 Rotation Sequences and Euler Angle Computation

Thirteen rotation sequences and the equations involved in each of the computations are given in the following.

3.2.1 Yaw-Pitch-Roll or Aerospace Rotation Sequence

This method is the same as that shown in section 2.3. It is listed here for completeness of this section and for ease of comparison with other methods. Equations (9) and (10), are repeated below.

$$\begin{bmatrix} g_x \\ g_y \\ g_z \end{bmatrix} = \begin{bmatrix} c\theta c\psi & c\theta s\psi & -s\theta \\ s\phi s\theta c\psi - c\phi s\psi & s\phi s\theta s\psi + c\phi c\psi & s\phi c\theta \\ c\phi s\theta c\psi + s\phi s\psi & c\phi s\theta s\psi - s\phi c\psi & c\phi c\theta \end{bmatrix} \begin{bmatrix} 0 \\ 0 \\ 1 \end{bmatrix} \quad (15)$$

$$\begin{bmatrix} m_x \\ m_y \\ m_z \end{bmatrix} = \begin{bmatrix} c\theta c\psi & c\theta s\psi & -s\theta \\ s\phi s\theta c\psi - c\phi s\psi & s\phi s\theta s\psi + c\phi c\psi & s\phi c\theta \\ c\phi s\theta c\psi + s\phi s\psi & c\phi s\theta s\psi - s\phi c\psi & c\phi c\theta \end{bmatrix} \begin{bmatrix} c\alpha \\ 0 \\ s\alpha \end{bmatrix}$$

$$\begin{aligned} \theta &= -\sin^{-1}(g_x) \\ \phi &= \sin^{-1}(g_y / \cos \theta) \\ \psi &= \cos^{-1}([m_x + \sin \theta \sin \alpha] / [\cos \theta \cos \alpha]) \end{aligned} \quad (16)$$

Aerospace rotation sequence Euler angles can be computed using the measurements - g_x , g_y and m_x . It is to be noted that any extraneous fields or a failure of any or all of the remaining sensor axes would not make a difference to the computation above. Since the computed rotation angles already correspond to the aerospace sequence, no further conversion is required.

3.2.2 Roll-Pitch-Yaw sequence (RPY)

Using the rotation matrix for the Roll-Pitch-Yaw sequence along with reference and final measurement vectors, the RPY rotation angles - θ_1 , ϕ_1 and ψ_1 can be computed. The

rotation matrix that relates the vectors are shown below followed by the inverse trigonometric functions to solve for the angles.

$$\begin{aligned} \begin{bmatrix} g_x \\ g_y \\ g_z \end{bmatrix} &= \begin{bmatrix} c\psi_1 c\theta_1 & s\psi_1 c\phi_1 + c\psi_1 s\theta_1 s\phi_1 & s\psi_1 s\phi_1 - c\psi_1 s\theta_1 c\phi_1 \\ -s\psi_1 c\theta_1 & c\psi_1 c\phi_1 - s\psi_1 s\theta_1 s\phi_1 & c\psi_1 s\phi_1 + s\psi_1 s\theta_1 c\phi_1 \\ s\theta_1 & -c\theta_1 s\phi_1 & c\theta_1 c\phi_1 \end{bmatrix} \begin{bmatrix} 0 \\ 0 \\ 1 \end{bmatrix} \\ \begin{bmatrix} m_x \\ m_y \\ m_z \end{bmatrix} &= \begin{bmatrix} c\psi_1 c\theta_1 & s\psi_1 c\phi_1 + c\psi_1 s\theta_1 s\phi_1 & s\psi_1 s\phi_1 - c\psi_1 s\theta_1 c\phi_1 \\ -s\psi_1 c\theta_1 & c\psi_1 c\phi_1 - s\psi_1 s\theta_1 s\phi_1 & c\psi_1 s\phi_1 + s\psi_1 s\theta_1 c\phi_1 \\ s\theta_1 & -c\theta_1 s\phi_1 & c\theta_1 c\phi_1 \end{bmatrix} \begin{bmatrix} \cos \alpha \\ 0 \\ \sin \alpha \end{bmatrix} \end{aligned} \quad (17)$$

$$\begin{aligned} \theta_1 &= \sin^{-1} \left(\frac{m_z - g_z \sin \alpha}{\cos \alpha} \right) \\ \phi_1 &= \cos^{-1} \left(\frac{g_z}{\cos \theta_1} \right) \\ \psi_1 &= \sin^{-1} \left(\frac{Bm_x - Am_y}{A^2 + B^2} \right) \end{aligned} \quad (18)$$

where,

$$\begin{aligned} A &= \cos \theta_1 \cos \alpha - \sin \theta_1 \cos \phi_1 \sin \alpha \\ B &= \sin \phi_1 \sin \alpha \end{aligned}$$

It can be observed from equations (15) and (17) that the input and output vectors are the same in both cases while the rotation matrices are different. Using the result from section 3.1, it can be said that the two rotation matrices of (15) and (17) are also equal.

Therefore,

$$\begin{aligned} \begin{bmatrix} c\theta c\psi & c\theta s\psi & -s\theta \\ s\phi s\theta c\psi - c\phi s\psi & s\phi s\theta s\psi + c\phi c\psi & s\phi c\theta \\ c\phi s\theta c\psi + s\phi s\psi & c\phi s\theta s\psi - s\phi c\psi & c\phi c\theta \end{bmatrix} &= \begin{bmatrix} c\psi_1 c\theta_1 & s\psi_1 c\phi_1 + c\psi_1 s\theta_1 s\phi_1 & s\psi_1 s\phi_1 - c\psi_1 s\theta_1 c\phi_1 \\ -s\psi_1 c\theta_1 & c\psi_1 c\phi_1 - s\psi_1 s\theta_1 s\phi_1 & c\psi_1 s\phi_1 + s\psi_1 s\theta_1 c\phi_1 \\ s\theta_1 & -c\theta_1 s\phi_1 & c\theta_1 c\phi_1 \end{bmatrix} \end{aligned} \quad (19)$$

Equating some of the individual elements from the above matrices we get,

$$\begin{aligned}
-\sin \theta &= \sin \phi_1 \sin \psi_1 - \cos \phi_1 \sin \theta_1 \cos \psi_1 \\
\cos \phi \cos \theta &= \cos \phi_1 \cos \theta_1 \\
\cos \theta \cos \psi &= \cos \psi_1 \cos \theta_1
\end{aligned}$$

Using the above equations, the Euler angles can be computed as,

$$\begin{aligned}
\theta &= \sin^{-1} (\cos \phi_1 \sin \theta_1 \cos \psi_1 - \sin \phi_1 \sin \psi_1) \\
\phi &= \cos^{-1} \left(\frac{\cos \theta_1 \cos \phi_1}{\cos \theta} \right) \\
\psi &= \cos^{-1} \left(\frac{\cos \theta_1 \cos \psi_1}{\cos \theta} \right)
\end{aligned} \tag{20}$$

Therefore using equations (18) and (20) along with sensor measurements - g_z , m_x , m_y and m_z , Euler angles corresponding to the YPR sequence can be computed. Moreover it is seen that, measurements g_x and g_y were not used. Thus any inertial accelerations or a failure of one or both of these axes sensors would not affect the Euler angles computed in this way.

3.2.3 Yaw-Roll-Pitch sequence (YRP)

The rotation matrices of the YRP sequence along with their respective reference and measurement vectors are shown below.

$$\begin{aligned}
\begin{bmatrix} g_x \\ g_y \\ g_z \end{bmatrix} &= \begin{bmatrix} c\psi_2 c\theta_2 - s\psi_2 s\theta_2 s\phi_2 & s\psi_2 c\theta_2 + c\psi_2 s\theta_2 s\phi_2 & -c\phi_2 s\theta_2 \\ -s\psi_2 c\phi_2 & c\psi_2 c\phi_2 & s\phi_2 \\ c\psi_2 s\theta_2 + c\theta_2 s\phi_2 s\psi_2 & s\psi_2 s\theta_2 - c\theta_2 s\phi_2 c\psi_2 & c\theta_2 c\phi_2 \end{bmatrix} \begin{bmatrix} 0 \\ 0 \\ 1 \end{bmatrix} \\
\begin{bmatrix} m_x \\ m_y \\ m_z \end{bmatrix} &= \begin{bmatrix} c\psi_2 c\theta_2 - s\psi_2 s\theta_2 s\phi_2 & s\psi_2 c\theta_2 + c\psi_2 s\theta_2 s\phi_2 & -c\phi_2 s\theta_2 \\ -s\psi_2 c\phi_2 & c\psi_2 c\phi_2 & s\phi_2 \\ c\psi_2 s\theta_2 + c\theta_2 s\phi_2 s\psi_2 & s\psi_2 s\theta_2 - c\theta_2 s\phi_2 c\psi_2 & c\theta_2 c\phi_2 \end{bmatrix} \begin{bmatrix} \cos \alpha \\ 0 \\ \sin \alpha \end{bmatrix}
\end{aligned} \tag{21}$$

Using (21), the rotation angles can be computed as

$$\begin{aligned}
\phi_2 &= \sin^{-1}(g_y) \\
\theta_2 &= \cos^{-1}\left(\frac{g_z}{\cos \phi_2}\right) \\
\psi_2 &= \sin^{-1}\left(\frac{m_y - \sin \phi_2 \sin \alpha}{\cos \phi_2 \cos \alpha}\right)
\end{aligned} \tag{22}$$

Now these angles can be converted to the YPR Euler angles using the algorithm of section 3.1. The equations which help in doing the same are shown below.

$$\begin{aligned}
\theta &= \sin^{-1}(\cos \phi_2 \sin \theta_2) \\
\phi &= \sin^{-1}\left(\frac{\sin \phi_2}{\cos \theta}\right) \\
\psi &= \cos^{-1}\left(\frac{\cos \psi_2 \cos \theta_2 - \sin \psi_2 \sin \theta_2 \sin \phi_2}{\cos \theta}\right)
\end{aligned} \tag{23}$$

It can be noticed from (22) that measurements utilized in this method are g_y , g_z and m_y .

3.2.4 Roll-Yaw-Pitch sequence (RYP)

The rotation matrix corresponding to the RYP sequence and the equations required to obtain the rotation angles θ_3 , ϕ_3 and ψ_3 are given below followed by the equation to convert these angles to YPR Euler angles. It is to be noted that this method requires the measurements - g_x , g_y , g_z and m_y .

$$\begin{bmatrix}
c\psi_3 c\theta_3 & s\psi_3 c\theta_3 c\phi_3 + s\phi_3 s\theta_3 & c\theta_3 s\phi_3 s\psi_3 - c\phi_3 s\theta_3 \\
-s\psi_3 & c\psi_3 c\phi_3 & c\psi_3 s\phi_3 \\
c\psi_3 s\theta_3 & s\psi_3 s\theta_3 c\phi_3 - c\theta_3 s\phi_3 & s\psi_3 s\theta_3 s\phi_3 + c\theta_3 c\phi_3
\end{bmatrix} \tag{24}$$

$$\begin{aligned}
\psi_3 &= \sin^{-1} \left(\frac{g_y \sin \alpha - m_y}{\cos \alpha} \right) \\
\phi_3 &= \sin^{-1} \left(\frac{g_y}{\cos \psi_3} \right) \\
\theta_3 &= \sin^{-1} \left(\frac{Ag_z - Bg_x}{A^2 + B^2} \right)
\end{aligned} \tag{25}$$

where,

$$\begin{aligned}
A &= \sin \phi_3 \sin \psi_3 \\
B &= \cos \phi_3
\end{aligned}$$

The rotation angles can be converted to the standard Euler angles using the following equations.

$$\begin{aligned}
\theta &= \sin^{-1} (\cos \phi_3 \sin \theta_3 - \cos \theta_3 \sin \phi_3 \sin \psi_3) \\
\phi &= \sin^{-1} \left(\frac{\cos \psi_3 \sin \phi_3}{\cos \theta} \right) \\
\psi &= \cos^{-1} \left(\frac{\cos \theta_3 \cos \psi_3}{\cos \theta} \right)
\end{aligned} \tag{26}$$

3.2.5 Pitch-Roll-Yaw sequence (PRY)

The rotation matrix for this system can be obtained by multiplying the rotation matrices for yaw shown in (5), roll shown in (7) and pitch shown in (6) in that order. Using the rotation matrix, the angles can be computed using the equations shown below.

$$\begin{aligned}
\theta_4 &= \tan^{-1} \left(\frac{m_z - g_z \sin \alpha}{g_z \cos \alpha} \right) \\
\phi_4 &= \cos^{-1} \left(\frac{g_z}{\cos \theta_4} \right) \\
\psi_4 &= \sin^{-1} \left(\frac{Ag_x + Bg_y}{A^2 + B^2} \right)
\end{aligned} \tag{27}$$

where,

$$A = \cos \theta_4 \sin \phi_4$$

$$B = \sin \theta_4$$

These angles are converted to standard Euler angles as follows,

$$\begin{aligned}\theta &= \sin^{-1}(\cos \psi_4 \sin \theta_4 - \cos \theta_4 \sin \phi_4 \sin \psi_4) \\ \phi &= \cos^{-1}\left(\frac{\cos \theta_4 \cos \phi_4}{\cos \theta}\right) \\ \psi &= \sin^{-1}\left(\frac{\sin \psi_4 \cos \phi_4}{\cos \theta}\right)\end{aligned}\tag{28}$$

It can be observed from (27) that knowledge of the sensor measurements - g_x , g_y , g_z and m_z are sufficient in the computation of Euler angles using this method.

3.2.6 Pitch-Yaw-Roll sequence (PYR)

The rotation angles associated with the pitch-yaw-roll sequence can be computed using equations that follow. Note that g_x , m_x , m_y and m_z are utilized in this computation.

$$\begin{aligned}\theta_5 &= \tan^{-1}\left(\frac{-g_x \cos \alpha}{m_x - g_x \sin \alpha}\right) \\ \psi_5 &= \cos^{-1}\left(\frac{-g_x}{\sin \theta}\right) \\ \phi_5 &= \cos^{-1}\left(\frac{Am_y + Bm_z}{A^2 + B^2}\right)\end{aligned}\tag{29}$$

where,

$$\begin{aligned}A &= \sin \psi_5 \sin \theta_5 \sin \alpha - \sin \psi_5 \cos \theta_5 \cos \alpha \\ B &= \sin \theta_5 \cos \alpha + \cos \theta_5 \sin \alpha\end{aligned}$$

These angles also need to be converted to standard Euler angles. This is done through the equations below.

$$\begin{aligned}
\theta &= \sin^{-1}(\cos \psi_5 \sin \theta_5) \\
\phi &= \sin^{-1}\left(\frac{\sin \psi_5 \sin \theta_5 \cos \phi_5 + \cos \theta_5 \sin \phi_5}{\cos \theta}\right) \\
\psi &= \sin^{-1}\left(\frac{\sin \psi_5}{\cos \theta}\right)
\end{aligned} \tag{30}$$

3.2.7 Yaw-Pitch-Roll-2 (YPR₂)

For the each of the rotation sequences discussed above, it is possible to compute Euler angles using different sets of equations and different sets of sensor measurements. One such alternative set of equations to compute Euler angles based on the YPR sequence is called as YPR₂. This is shown in (31). The angle computation equations are derived from the YPR rotation matrix shown in (15). These are:

$$\begin{aligned}
\phi &= \tan^{-1}\left(\frac{g_y}{g_z}\right) \\
\theta &= \cos^{-1}\left(\frac{g_y}{\sin \phi}\right) \\
\psi &= \sin^{-1}\left(\frac{A(m_z - D) - E(m_y - C)}{(BE + AF)}\right)
\end{aligned} \tag{31}$$

where,

$$\begin{aligned}
A &= (\sin \phi)(\sin \theta)(\cos \alpha) \\
B &= (\cos \phi)(\cos \alpha) \\
C &= (\sin \phi)(\cos \theta)(\sin \alpha) \\
D &= (\cos \phi)(\cos \theta)(\sin \alpha) \\
E &= (\cos \phi)(\sin \theta)(\cos \alpha) \\
F &= (\sin \phi)(\cos \alpha)
\end{aligned}$$

It is seen from equation (31) that this computation depends on g_y , g_z , m_y and m_z .

Similarly alternative equation sets can be developed for each of the rotation sequences shown in sections 3.2.2 to 3.2.6.

3.2.8 Yaw-Pitch-Yaw sequence (YPY)

This rotation involves two non-consecutive rotations about the same axis and the other rotation is about one of the remaining axes. As the name suggests this rotation consists of a yaw followed by a pitch and then another yaw. The two yaw rotations are considered to be through angles ψ_6 and ψ_7 while the pitch is about θ_6 . The rotation matrix is as shown in (32).

$$\begin{bmatrix} c\psi_7 c\theta_6 c\psi_6 - s\psi_6 s\psi_7 & c\psi_7 c\theta_6 s\psi_6 + s\psi_7 c\psi_6 & -c\psi_7 s\theta_6 \\ -s\psi_7 c\theta_6 c\psi_6 - c\psi_7 s\psi_6 & c\psi_7 c\psi_6 - s\psi_7 c\theta_6 s\psi_6 & s\psi_7 s\theta_6 \\ s\theta_6 c\psi_6 & s\theta_6 s\psi_6 & c\theta_6 \end{bmatrix} \quad (32)$$

Using the above rotation matrix, along with the measurements of acceleration and magnetic field, the rotation angles are found as

$$\begin{aligned} \psi_7 &= \tan^{-1} \left(\frac{-g_y}{g_x} \right) \\ \theta_6 &= \sin^{-1} \left(\frac{g_y}{\sin \psi_7} \right) \\ \psi_6 &= \cos^{-1} \left(\frac{m_z - \cos \theta_6 \sin \alpha}{\cos \alpha \sin \theta_6} \right) \end{aligned} \quad (33)$$

Since the above angles are not standard Euler angles, they are converted through the equation shown below. g_x , g_y and m_z are used in this computation.

$$\begin{aligned}
\theta &= \sin^{-1}(\cos \psi_7 \sin \theta_6) \\
\phi &= \cos^{-1}\left(\frac{\cos \theta_6}{\cos \theta}\right) \\
\psi &= \cos^{-1}\left(\frac{\cos \psi_7 \cos \theta_6 \cos \psi_6 - \sin \psi_7 \sin \psi_6}{\cos \theta}\right)
\end{aligned} \tag{34}$$

3.2.9 Yaw-Roll-Yaw sequence (YRY)

This rotation is similar to the previous one where the two non-consecutive rotations are considered about the yaw axis and another about the roll axis. The computation equations are shown below.

$$\begin{aligned}
\psi_9 &= \tan^{-1}\left(\frac{g_x}{g_y}\right) \\
\phi_6 &= \sin^{-1}\left(\frac{g_x}{\sin \psi_9}\right) \\
\psi_8 &= \sin^{-1}\left(\frac{m_z - \cos \phi_6 \sin \alpha}{\cos \alpha \sin \phi_6}\right)
\end{aligned} \tag{35}$$

$$\begin{aligned}
\theta &= -\sin^{-1}(\sin \psi_9 \sin \phi_6) \\
\phi &= \cos^{-1}\left(\frac{\cos \phi_6}{\cos \theta}\right) \\
\psi &= \cos^{-1}\left(\frac{\cos \psi_9 \cos \psi_8 - \sin \psi_9 \cos \phi_6 \sin \psi_8}{\cos \theta}\right)
\end{aligned} \tag{36}$$

3.2.10 Roll-Pitch-Roll sequence (RPR)

The rotation angles associated with the roll-pitch-roll sequence can be computed as shown below. Note that g_x , m_x , m_y and m_z are utilized in this computation.

$$\begin{aligned}
\theta_7 &= \cos^{-1} \left(\frac{m_x - g_x \sin \alpha}{\cos \alpha} \right) \\
\phi_7 &= \cos^{-1} \left(\frac{g_x}{-\sin \theta_7} \right) \\
\phi_8 &= \cos^{-1} \left(\frac{Am_z + Bm_y}{A^2 + B^2} \right)
\end{aligned} \tag{37}$$

where,

$$\begin{aligned}
A &= \sin \theta_7 \cos \alpha + \cos \theta_7 \cos \phi_7 \sin \alpha \\
B &= \sin \phi_7 \sin \alpha
\end{aligned}$$

The above rotation angles can be converted to the standard Euler angles as:

$$\begin{aligned}
\theta &= \sin^{-1} (\sin \theta_7 \cos \phi_7) \\
\psi &= \cos^{-1} \left(\frac{\cos \theta_7}{\cos \theta} \right) \\
\phi &= \sin^{-1} \left(\frac{\cos \phi_8 \sin \phi_7 + \sin \phi_8 \cos \theta_7 \cos \phi_7}{\cos \theta} \right)
\end{aligned} \tag{38}$$

3.2.11 Roll-Yaw-Roll sequence (RYR)

The rotation angles associated with the roll-yaw-roll sequence can be found as follows.

$$\begin{aligned}
\psi_{10} &= \cos^{-1} \left(\frac{m_x - g_x \sin \alpha}{\cos \alpha} \right) \\
\phi_9 &= \sin^{-1} \left(\frac{g_x}{\sin \psi_{10}} \right) \\
\phi_{10} &= \sin^{-1} \left(\frac{Am_z + Bm_y}{A^2 + B^2} \right)
\end{aligned} \tag{39}$$

where,

$$\begin{aligned}
A &= \sin \psi_{10} \cos \alpha - \cos \psi_{10} \sin \phi_9 \sin \alpha \\
B &= \cos \phi_9 \sin \alpha
\end{aligned}$$

The above rotation angles are computed using the measurements g_x , m_x , m_y and m_z .

They can be converted to the standard Euler angles using the following equations.

$$\begin{aligned}
\theta &= -\sin^{-1}(\sin \psi_{10} \sin \phi_9) \\
\psi &= \cos^{-1}\left(\frac{\cos \psi_{10}}{\cos \theta}\right) \\
\phi &= \sin^{-1}\left(\frac{\sin \phi_{10} \cos \phi_9 + \cos \phi_{10} \cos \psi_{10} \sin \phi_9}{\cos \theta}\right)
\end{aligned} \tag{40}$$

3.2.12 Pitch-Roll-Pitch sequence (PRP)

The rotation angles associated with the pitch-roll-pitch sequence can be computed and then converted to standard Euler angles as shown in the following.

$$\begin{aligned}
\theta_8 &= \tan^{-1}\left(\frac{m_y - g_y \sin \alpha}{g_y \cos \alpha}\right) \\
\phi_{11} &= \sin^{-1}\left(\frac{g_y}{\cos \theta_8}\right) \\
\theta_9 &= \cos^{-1}\left(\frac{Am_z + Bm_x}{A^2 + B^2}\right)
\end{aligned} \tag{41}$$

where,

$$\begin{aligned}
A &= \cos \phi_{11} \sin \theta_8 \cos \alpha + \cos \phi_{11} \cos \theta_8 \sin \alpha \\
B &= \cos \theta_8 \cos \alpha - \sin \theta_8 \sin \alpha \\
\theta &= \sin^{-1}(\cos \theta_9 \sin \theta_8 + \sin \theta_9 \cos \phi_{11} \cos \theta_8) \\
\phi &= \sin^{-1}\left(\frac{\sin \phi_{11} \cos \theta_8}{\cos \theta}\right) \\
\psi &= \sin^{-1}\left(\frac{\sin \theta_9 \sin \phi_{11}}{\cos \theta}\right)
\end{aligned} \tag{42}$$

The measurements g_y , m_x , m_y and m_z are used in the computation.

3.2.13 Pitch-Yaw-Pitch sequence (PYP)

The rotation angles associated with the pitch-yaw-pitch sequence can be computed as follows.

$$\begin{aligned}
\theta_{10} &= \tan^{-1} \left(\frac{g_y \cos \alpha}{g_y \sin \alpha - m_y} \right) \\
\psi_{11} &= \sin^{-1} \left(\frac{g_y}{\sin \theta_{10}} \right) \\
\theta_{11} &= \cos^{-1} \left(\frac{Am_x + Bm_z}{A^2 + B^2} \right)
\end{aligned} \tag{43}$$

where,

$$\begin{aligned}
A &= \cos \psi_{11} \cos \theta_{10} \cos \alpha - \cos \psi_{11} \sin \theta_{10} \sin \alpha \\
B &= \sin \theta_{10} \cos \alpha + \cos \theta_{10} \sin \alpha
\end{aligned}$$

The above rotation angles are computed using the measurements g_y , m_x , m_y and m_z .

They can be converted to the standard Euler angles using the following equations.

$$\begin{aligned}
\theta &= \sin^{-1} (\cos \theta_{11} \sin \theta_{10} \cos \psi_{11} + \sin \theta_{11} \cos \theta_{10}) \\
\phi &= \sin^{-1} \left(\frac{\sin \psi_{11} \sin \theta_{10}}{\cos \theta} \right) \\
\psi &= \sin^{-1} \left(\frac{\cos \theta_{11} \sin \psi_{11}}{\cos \theta} \right)
\end{aligned} \tag{44}$$

3.3 Fault Tolerance in Attitude Determination

It has been shown in the previous section that Euler angles can be computed using the diversified redundant formulas based on different subsets of measurements. Thirteen different Euler angle computation methods were presented and it is possible to develop at least twelve more. Table 1 lists the different subsets of sensor measurement data required for each of the twenty five variations. Provided that all the sensors are in good health and none of them are affected by any disturbance, all twenty-five methods produce the same Euler angle results. If an individual sensor axis is faulty or affected by disturbances, some of the computational methods give consistent and identical results, while the other results would be inconsistent and incorrect. As an example if the sensor measuring the x -

direction acceleration or g_x is affected by an inertial acceleration e_x , the Euler angles calculated using YPR, YPR₃, YPR₄, YPR₅, RPY₂, YRP₂, YRP₃, RYP, PRY, PYR, PYR₂, YPY, YPY₂, YRY, YRY₂, RPR, and RYR methods are affected. Each of the above methods produces incorrect results. Moreover all of them are inconsistent with each other. All the other methods – YPR₂, YPR₆, RPY, YRP, YRP₄, RYP₂, PRY₂, PRP and PYP continue to produce correct Euler angle results. These results are also seen to be consistent with each other. One common factor that can be observed among them is that all the methods which produce consistent results do not utilize the measurement of the x direction acceleration.

Observing that nine out of the twenty five methods produce consistent results while the remaining sixteen are inconsistent with each other, a simple algorithm like majority voting among all the available results would suffice in identifying the correct Euler angles. By identifying the correct Euler angles, it is possible to eliminate the effect of the disturbance - extraneous acceleration thus improving fault tolerant.

In case of a failure or an extraneous magnetic field disturbance affecting the magnetic field sensor of the y direction i.e. m_y , rotation sequences like YPR, YPR₃, YPR₆, RPY₂, YRP₂, YRP₃, YRP₄, PRY₂, PRY, PYR₂, YPY and YRY will remain unaffected and produce correct and consistent results. All the other sequences which utilize this measurement are all affected in different ways such that they produce incorrect and inconsistent results.

This diversified redundant computing approach can be extended to diagnose failures or extraneous effects on sets of two sensors as well. For example, if accelerometer y and z axes are affected by inertial accelerations, it is seen that PYR, RPR and RYR sequence

computations remain unaffected. They are also seen to produce consistent results whereas all the other methods produce inconsistent and incorrect results. Thus a failure on each sensor has a characteristic effect on the results produced. This unique “*fingerprint*” left by the failed sensor or sensors helps in its identification. It is also possible to calculate the magnitude of the contaminating field. The procedure of this computation will be explained through an example later in this document.

Table 1. Different computation methods and sensor axes used

	g_x	g_y	g_z	m_x	m_y	m_z
YPR	X	X		X		
YPR₂		X	X		X	X
YPR₃	X		X	X		
YPR₄	X	X			X	X
YPR₅	X		X		X	X
YPR₆		X	X	X		
RPY			X	X	X	X
RPY₂	X	X	X			X
YRP		X	X		X	
YRP₂	X		X		X	
YRP₃	X		X	X		X
YRP₄		X	X	X		X
RYP	X	X	X		X	
RYP₂		X		X	X	X
PRY	X	X	X			X
PRY₂			X	X	X	X
PYR	X			X	X	X
PYR₂	X	X	X	X		
YPY	X	X				X
YPY₂	X	X		X	X	
YRY	X	X				X
RPR	X			X	X	X
RYR	X			X	X	X
PRP		X		X	X	X
PYP		X		X	X	X

Provided that the UAV has room for a few more sensors, the rate gyro can be employed. Together with the flight dynamics model, the observer and Kalman filter theory it can be used to estimate the Euler angles. Although this estimation may not be as accurate, it can serve as a backup when the magnetometer and accelerometer sensors fail or are contaminated with extraneous fields to a point where none of the equations (16) to (44) can help in producing correct Euler angles.

3.4 Computational Issues

Inverse trigonometric functions have some inherent numerical difficulties associated with them. Two of them – singularity and ambiguity are discussed in this section. These problems can be overcome and in some cases they can even be used to our advantage as will be shown in the following.

3.4.1 Singularity

In the Euler angle computation formulations given above, one important issue is the singularity that occurs when a denominator of a rational function becomes zero. In addition to the computational difficulties at the singularity point, it is found that in some of the computation methods, the computation of inverse trigonometric functions becomes less numerically stable and more sensitive to sensor measurement uncertainties as the vehicle attitude tends towards a singularity point whereas other methods remain stable and reliable at the same angles.

As an example, when the pitch of the vehicle tends towards 90° , it is seen that YPR and PYR computation formulas give incorrect Euler angles even when the sensor measurements are contaminated with very slight noises. Other methods like YPR_2 are

seen to be more stable at the same range of angles. Table 2 shows how sensor noises around this position affect the Euler angle computations. The triple inside the braces $\{\theta, \phi, \psi\}$ represent pitch, roll, and yaw angles in degrees. The Euler angles under the “Actual” column represent the actual attitude of the vehicle, and those in Columns 2 to 4 are computed based on the six sensor measurements contaminated with random noises so that the sensor data used for computation are deviated from their originals by about $\pm 1\%$.

Table 2. Effect of Singularity & sensor noise.

Actual	YPR	YPR ₂	PYR
$\{15, 30, 45\}$	$\{15.1, 29.7, 44.8\}$	$\{16.8, 30, 44.3\}$	$\{15.1, 31.9, 44.8\}$
$\{60, 30, 45\}$	$\{59.7, 30, 46.1\}$	$\{59.8, 30, 44.9\}$	$\{59.7, 29.1, 46.1\}$
$\{75, 30, 45\}$	$\{74.8, 29.7, 43.9\}$	$\{74.9, 30, 45.4\}$	$\{74.8, 28, 43.9\}$
$\{85, 30, 45\}$	$\{81.5, 17, 72.5\}$	$\{85, 29.8, 44.8\}$	$\{81.5, 51.4, 72.5\}$

It can be seen that the Euler angles computed based on YPR, YPR₂, and PYR approaches match the actual ones closely when the pitch angle is less than 75° . But the effect of singularity and sensor noises increases as the pitch angle gets closer towards the singularity point of $\theta = 90^\circ$. YPR and PYR approaches start to fail when the pitch angle exceeds 85° . However, the YPR₂ approach continues to give reasonably accurate Euler angles results even when the pitch angle reaches 89° and the measurement noise level is increased to $\pm 5\%$. With the actual attitude at $\theta = 89^\circ$, $\phi = 30^\circ$ and $\psi = 45^\circ$, and the random noise level five times higher than the condition under which the data of Table 2 were obtained, the YPR₂ approach still delivers the following impressively close Euler

angles $\theta = 88.98^\circ$, $\phi = 29.94^\circ$ and $\psi = 45.12^\circ$. YPR₂ approach is robust around the point $\theta = 90^\circ$, but other approaches in Table 1 may be better in terms of numerical stability around other critical points like $\phi = 0^\circ$.

Singularity is an inconvenience involved in all inverse trigonometric functions. But since the singularities can be predicted before hand, it could be utilized towards our advantage in the majority voting algorithm. Before hand knowledge that the YPR and PYR methods are less reliable whenever pitch angle approaches 90° could be made a factor in the majority voting algorithm. This could actually help filter out some of the predictable and unreliable results like YPR and PYR from affecting the voting pattern whenever θ approaches 90° .

Use of additional sensors like rate gyro can also help alleviate this problem to a certain extent. The performance can also be improved if the random noises on the sensor measurement can be reduced.

3.4.2 Inverse Trigonometric Function Ambiguities / Quadrant Selection

The equations required for the computation of Euler angles involve inverse trigonometric functions. All the formulas involved in Euler angle computation involve three or six inverse trigonometric functions, and the solution of each function can be in one of two possible quadrants. If the quadrant is wrongly chosen at any of the steps, the final Euler angle computed would be incorrect.

As an example, consider a case where $g_z = 0.6124$, $m_x = -0.4356$, $m_y = 0.01957$, $m_z = 0.8999$ and $\alpha = 60^\circ$, then from equation (29) of the PYR approach we have the following possible solutions

$$\theta_5 = 63.44^\circ \text{ or } 243.44^\circ, \phi_5 = 20.77^\circ \text{ or } -20.77^\circ, \psi_5 = 37.76^\circ \text{ or } -37.77^\circ$$

Initially, we may have a rough estimate of the Euler angles θ , ϕ , and ψ obtained either through additional sensors or by virtue of pre-launch position of the vehicle, but not for the intermediate rotation angles θ_5 , ϕ_5 , and ψ_5 . There are six combinations for the solutions of the intermediate rotation angles, but only one would render the correct Euler angles. The above set of solutions can be plugged into (30) one by one until Euler angles are found to be close to the initial rough estimate, say $\theta_{est} \cong 43^\circ$, $\phi_{est} \cong 29^\circ$ and $\psi_{est} \cong 62^\circ$.

Plugging the following

$$\theta_5 = 63.44^\circ, \phi_5 = 20.77^\circ, \psi_5 = 37.76^\circ$$

into (30) produces possible Euler angle solutions as follows:

$$\theta = 45^\circ \text{ or } 135^\circ, \phi = 72^\circ \text{ or } 118^\circ, \psi = 60^\circ \text{ or } 120^\circ$$

Note that $\theta = 45^\circ$ and $\psi = 60^\circ$ are close to the known initial estimate, but neither $\phi = 72^\circ$ nor 118° is close. Now trying another set of intermediate rotation angles,

$$\theta_5 = 63.44^\circ, \phi_5 = -20.77^\circ, \psi_5 = 37.76^\circ$$

into (30) and we obtain the following possible solution:

$$\theta = 45^\circ \text{ or } 135^\circ, \phi = 30^\circ \text{ or } 150^\circ, \psi = 60^\circ \text{ or } 120^\circ$$

In the above Euler angles $\theta = 45^\circ$, $\phi = 30^\circ$, and $\psi = 60^\circ$ are close to the initial estimates.

Thus it can be concluded that $\theta_5 = 63.44^\circ$, $\phi_5 = -20.77^\circ$, $\psi_5 = 37.76^\circ$ are the correct set of intermediate rotation angles.

This trial and error process is only required once in the very beginning. After that, the intermediate rotation angles and Euler angles obtained during the present sampling period can be employed to correctly choose the relevant angles in the next sampling period.

Thus given the initial Euler angles and assuming the sampling period is small enough that these angles do not change abruptly within one sampling period, the quadrants for the rotation and Euler angles at the next sampling instant can be predicted. The initial Euler angles here do not need to be very accurate; hence, the estimation of Euler angles can also be based on the roll, pitch, and yaw rates measured by rate gyros. This can serve the purpose of quadrant selection.

4. EULER ANGLE COMPUTATION OF NASA GTM UAV ON A BANK-TO-TURN MANEUVER

In this chapter a multivariable controller is developed to control a NASA GTM UAV such that it banks through a particular angle while maintaining other parameters constant. Later the simulated bank-to-turn maneuver of the UAV is employed to demonstrate the fault tolerant computation of Euler angles under inertial acceleration interferences.

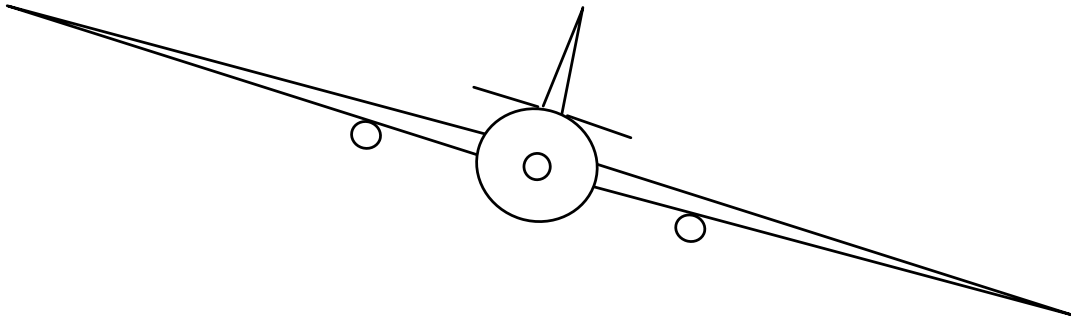


Figure 4. UAV bank-to-turn maneuver.

4.1 NASA GTM UAV System Dynamic Model and Controller Development

The UAV's dynamic model is obtained from wind tunnel data. The decoupled lateral dynamics mathematical model of the UAV can be given as:

$$UAV \text{ lateral } \begin{cases} \dot{x}(t) = Ax(t) + B_2 u(t) \\ y(t) = C_2 x(t) + D_{22} u(t) \end{cases} \quad (45)$$

with $x(t)$, $u(t)$ and $y(t)$ being state, control input, and output vectors, respectively.

$$x(t) = \begin{bmatrix} \beta \\ p \\ q \\ \phi \end{bmatrix} \quad u(t) = \begin{bmatrix} \delta_a \\ \delta_r \end{bmatrix} \quad y(t) = [\phi] \quad (46)$$

where, β is the side slip angle, p is the roll rate, q is the rate change of yaw, ϕ is the roll angle, δ_a is the aileron angle and rudder angle is given by δ_r .

In addition, disturbances $w_d(t)$ and noises $v(t)$ affect the system. These are assumed white noises with co-variances

$$E(w_d w_d^T) = I_4 \quad E(v v^T) = I_2 \quad E(w_d v^T) = 0$$

where, I_4 and I_2 are unity matrices of dimensions 4 and 2 respectively. These disturbances and noises are accounted for in the mathematical model through the more complete system model shown in (47).

$$\begin{aligned} \dot{x}(t) &= Ax(t) + B_1 w_d(t) + B_2 u(t) \\ y(t) &= C_2 x(t) + D_{21} v(t) + D_{22} u(t) \end{aligned} \quad (47)$$

It is required that the aircraft tracks the reference roll angle $r(t)$. This is accommodated through a regulator design. The regulator variable z is generated as:

$$z = \begin{bmatrix} z_1 \\ z_2 \end{bmatrix} = \begin{bmatrix} C_{1u} \\ 0 \end{bmatrix} x(t) + \begin{bmatrix} D_{11u} \\ 0 \end{bmatrix} r(t) + \begin{bmatrix} 0 \\ D_{12d} \end{bmatrix} u(t) \quad (48)$$

A controller needs to be designed for the overall dynamic model such that the bank-to-turn maneuver is accomplished. But the aircraft is a non-linear system. This non-linear model is linearized around the operating region. The operating region in the given simulation is –

UAV is considered to be flying at an altitude of 600 ft.

UAV speed is constant at 126.67 ft/sec.

The thrust level is around 15.06%.

The aircraft maintains level flight with angle of attack α and pitch angle θ at 4.71° .

Side slip angle β is maintained at -0.04° .

Roll rate, pitch rate and yaw rate are all maintained at 0.

The regulator variable z from (48) that needs to be minimized is such that z_1 is the difference between the reference r and the actual roll angle ϕ and z_2 represents control inputs from aileron and rudder which are to be minimized.

The mathematical model of the lateral dynamics of the aircraft linearized around this trim condition is shown below.

$$\begin{aligned}
 A &= \begin{bmatrix} -0.5738 & 0.0830 & -0.9835 & 0.2531 \\ -79.4227 & -5.4361 & 1.9811 & 0 \\ 28.264 & -0.2811 & -1.3997 & 0 \\ 0 & 1 & 0.0824 & 0 \end{bmatrix} & B_2 &= \begin{bmatrix} -0.00017 & 0.00335 \\ -0.7511 & 0.25156 \\ -0.02295 & -0.4041 \\ 0 & 0 \end{bmatrix} \\
 B_1 &= (10e-2)I_4 & C_2 &= [0 \ 0 \ 0 \ 1] & D_{22} &= [0] \\
 D_{21} &= [10e-8] & D_{11u} &= [1] & C_{1u} &= [0 \ 0 \ 0 \ -1] \\
 D_{12d} &= I_2
 \end{aligned} \tag{49}$$

A MIMO (multi input multi output) state feedback controller and a regulator are designed for this system such that the aircraft is stabilized and it tracks the roll angle reference command as closely as possible. The controller is designed with some important criteria in mind. They are

- i) The closed-loop system is internally stable,
- ii) The tracking error is zero at steady state, i.e.,

$$\lim_{t \rightarrow \infty} z_1(t) = 0$$

- iii) The following performance index is minimized,

$$J = \lim_{T \rightarrow \infty} \frac{1}{T} E \left[\int_0^T z^T(t) z(t) dt \right]$$

where $E[X]$ stands for the expected value of X .

The closed loop system the controller - K can be as shown in Figure 5.

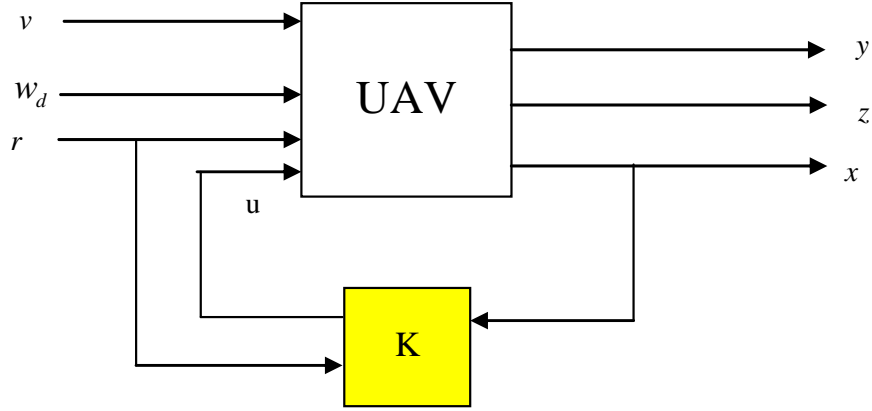


Figure 5. Generalized UAV plant and controller K in closed loop.

The multi-variable controller shown as K in Figure 5 has the structure shown below.

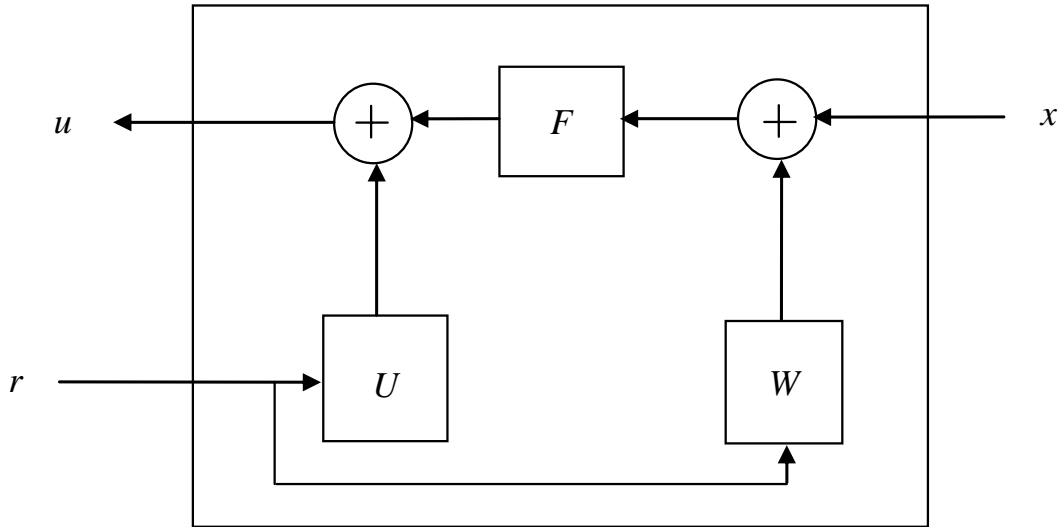


Figure 6. Structure of multi-variable controller K .

The reference roll angle r is in the form of a step signal of any particular value.

Therefore it is of the form

$$\dot{r}(t) = Zr(t) \quad \text{with} \quad Z = 0 \quad (50)$$

Well established control system design techniques like H_2 control theory along with regulator theory are used in the formulation of the state feedback matrix F and the regulator matrices U and W .

The condition for the existence of a stabilizing controller is that the system (A, B_2, C_2) is stabilizable and detectable. Once this condition has been established, construction of the U and W matrices for steady state regulation can be done such that (51) and (52) are satisfied.

$$AW + B_2U - WZ = 0 \quad (51)$$

$$C_{1u}W + D_{11u} = 0 \quad (52)$$

For the given UAV described by (49), numerical values of U and W were computed and found to be

$$U = \begin{bmatrix} -0.4391 \\ 0 \end{bmatrix} \quad (53)$$

$$W = \begin{bmatrix} 0.0118 \\ -0.0205 \\ 0.2489 \\ 1 \end{bmatrix} \quad (54)$$

In order to compute the state feedback matrix F , two matrices Q and R are defined as shown below.

$$\begin{aligned} Q &= C_{1u}^T C_{1u} \\ R &= D_{12d}^T D_{12d} \end{aligned} \quad (55)$$

Then the state feedback gain F can be computed as

$$F = -R^{-1} B_2^T X \quad (56)$$

where, X is the positive semi-definite stabilizing solution of the algebraic Riccati equation,

$$A^T X + XA - XB_2 R^{-1} B_2^T X + Q = 0 \quad (57)$$

The numerical value of F is obtained as:

$$F = \begin{bmatrix} -0.9193 & 0.2508 & 0.5492 & 1.2406 \\ -0.8543 & 0.1855 & 0.9918 & 1.1861 \end{bmatrix} \quad (58)$$

The controller with the structure shown in Figure 6 is constructed using the matrices U , W and F computed above.

The closed loop system is simulated with the reference roll angle given as a step input of magnitude 5° . This induces a bank motion on the UAV such that it gradually proceeds into a steady state roll angle of 5° . This banking causes it to follow a circular path such that its yaw angle is continuously increasing. The UAV is also controlled such that it maintains a constant altitude. The measurement data from simulation are utilized in further analysis and angle computation.

4.2 Euler Angle Computation with Disturbance Affected Accelerometer

A 3-axis accelerometer and a 3-axis magnetometer are mounted on the UAV according to the configuration shown in Figure 3. The x axis of each sensor is along the body and pointing towards the front, y axis is pointing towards the right and z is pointing towards the ground. A MEMS rate gyro is also mounted on the UAV to measure the rate of angle change. During steady level flight with no inertial acceleration or magnetic field disturbances, these sensors purely record measurements of earth gravity and magnetic fields. However, once it enters the bank-to-turn motion, it is in moving in a circular path.

This causes the UAV to experience inertial accelerations in the form of a persistent centrifugal acceleration along its y and z directions. Figure 7 shows the accelerometer measurements from the simulation. The magnetometer measurements are shown in Figure 8.

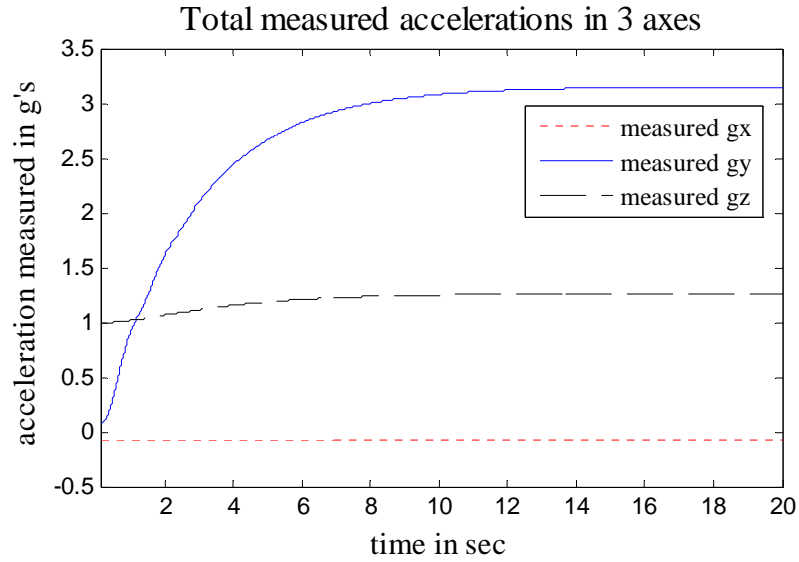


Figure 7. Accelerometer measurements from simulation.

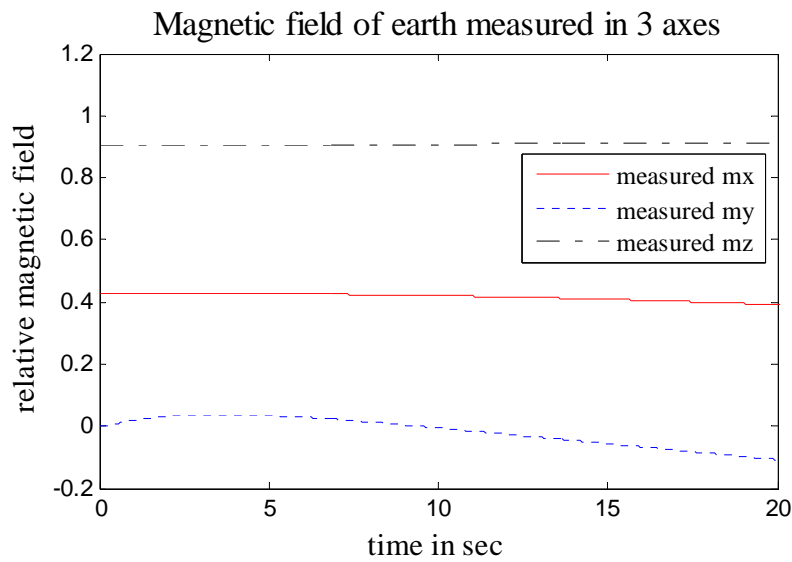


Figure 8. Simulated magnetic field measurement.

The measurement data from the above graphs are utilized to compute Euler angles through all the Euler angle computation formulas shown in equations (16) to (44). Some of the computation results at time instants 0.2 sec, 3 sec and 10 sec are shown in Table 3, Table 4 and Table 5 respectively.

Table 3. Euler angles computed at time instant 0.3 sec.

	θ	ϕ	ψ
YPR	4.71	4.9287	0.0482
RPY	4.7062	0.2109	0.2659
RYP	4.7127	4.9287	8.8494
PYR	4.712	0.094	0.048
RPR	4.708	0.091	0.0485
RYR	4.7	0.09	0.0478
PRP	2.5915	4.9171	0.255
PYP	55.2783	8.1255	14.6407

Table 4. Euler angles computed at time instant 3 sec.

	θ	ϕ	ψ
YPR	4.71	$90 - 78.8i$	1.6606
RPY	$-6.7 + 0.2i$	$0.4 + 3.4i$	$3.6 - 3.6i$
RYP	$-1 + 100i$	$36.9 - 0.7i$	$89.7 - 56.7i$
PYR	4.712	3.327	1.665
RPR	4.7	3.323	1.66
RYR	4.715	3.3227	1.6616
PRP	$-1.6 + 94i$	$61.5 + 3.58i$	$88.3 - 14.8i$
PYP	$10.75 + 80i$	$64.5 + 21.1i$	$79.6 + 66.5i$

Table 5. Euler angles computed at time instant 10 sec.

	θ	ϕ	ψ
YPR	4.71	$90 - 102i$	9.4929
RPY	$-17 - 0.12i$	$0.14 + 16i$	$0.46 + 7.7i$
RYP	$-1 + 100i$	$36.9 - 0.7i$	$89.7 - 56.7i$
PYR	4.72	4.888	9.4899
RPR	4.715	4.885	9.491
RYR	4.709	4.8823	9.495
PRP	$0.6 + 106i$	$69.8 + 1.75i$	$89.4 - 5.55i$
PYP	$6.97 + 99.9i$	$73.3 + 23.2i$	$82.1 + 72.1i$

It is seen from the above tables that the PYR, RPR and RYR methods produced consistent results while all the others produced results which are inconsistent with each other. The results from those methods not shown in the above tables are also seen to be inconsistent. It can be seen from Table 1 that one common factor among the methods which produce consistent results - PYR, RPR and RYR is that all these three methods do not utilize the measurements g_y and g_z while all the other methods utilize one or both these measurements. This characteristic “*fingerprint*” of the results leads us to the conclusion that both the measurements g_y and g_z are in error. This is verified by examining the accelerometer measurement graph in Figure 7. This graph shows that g_y measures nearly three times the normal gravity or $3g$ while g_z measures an acceleration which is slightly more than the gravity of earth. These are abnormally large and confirms our inference that measurements g_y and g_z are in error. This disturbance on the measurements was caused by centrifugal acceleration acting in the y and z directions of the UAV body when it went through the bank-to-turn circular motion.

Despite utilizing such disturbance ridden sensor measurements, a majority vote among all the computed Euler angle results has lead us to the correct Euler angles. Thus it is possible to eliminate the effect of disturbances on certain sets of sensors thus making the sensor system more robust. Utilizing multiple rotation sequences to compute the Euler angles has thus created a new type of redundancy called diversified redundancy. This redundancy has provided the fault tolerance thus helping in obtaining the correct Euler angles despite certain parts of the measurement vectors being in error.

Further examination of these three methods reveals that they produce valid and consistent Euler angle results throughout the time interval 0 to 20 sec. The results from all three methods are almost identical and this is shown in the graph of Figure 9.

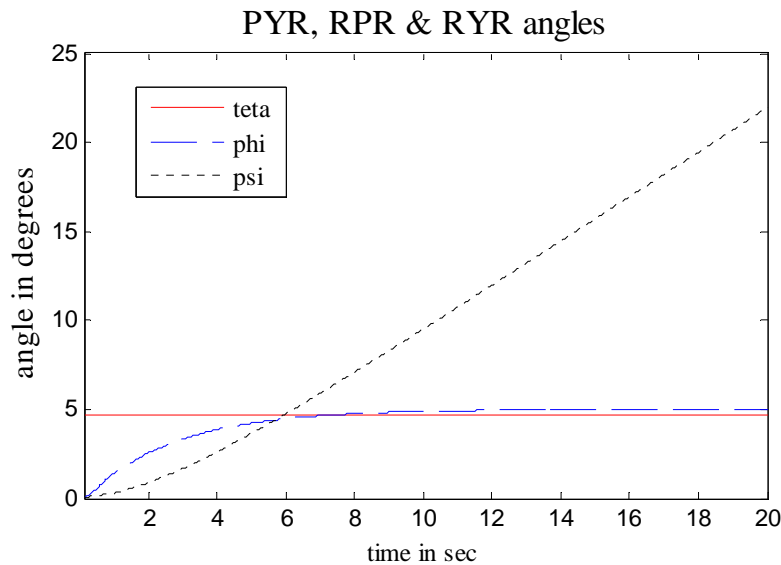


Figure 9. Euler angle results from the PYR, RPR & RYR rotation sequences

Figure 9 accurately describes the banking and circular motion of the UAV, where the pitch is maintained at 4.71° , roll angle tends towards 5° . This roll causes banking which

in turn causes the yaw angle to increase. This monotonically increasing yaw is indicative of circular motion.

It should be observed from Table 3, Table 4 and Table 5 that PRP and PYP computation methods have produced inconsistent results. This despite the fact that both these methods utilize the exact same set of measurements - g_y , m_x , m_y and m_z . A preliminary examination of the equations (41) to (44) shows that even though the same sensor set is utilized, the individual measurements are utilized differently in both these computation methods. This in turn causes inconsistency among the results when one or more of the measurements are at fault.

In addition to improving robustness of the sensor system, the proposed approach can also be employed to compute the value of the inertial accelerations that affected the sensors in the first place. This can be done by using the correct Euler angles obtained from the majority vote to reconstruct the true components of gravity and/or magnetic field. This can be done by substituting the correct θ , ϕ and ψ into the equation (9). However, the reconstructed gravity field components from time between 0 and 20 sec are shown in Figure 10. In this example the magnetic field is unaffected. Thus the values and the graph shown in Figure 8 continues to be valid.

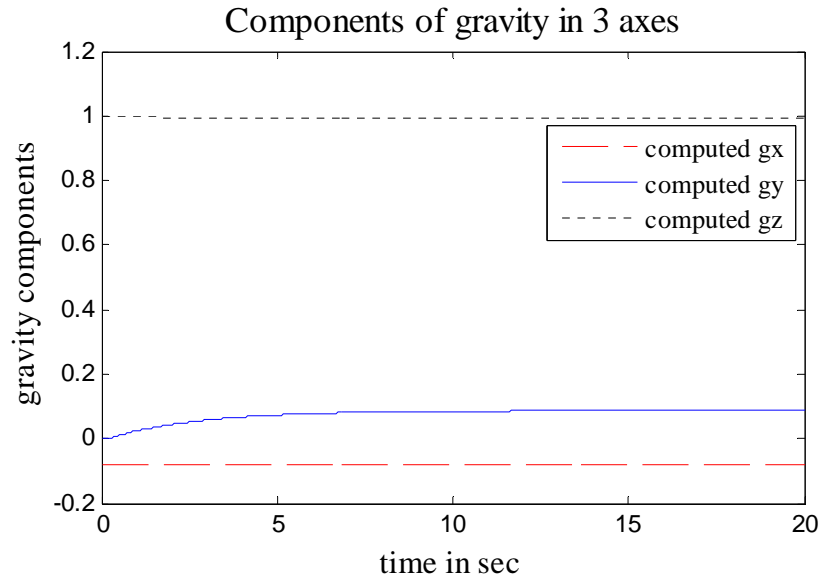


Figure 10. Gravity components reconstructed from Euler angles

Subtracting corresponding measurements of the graph in Figure 10 from those in Figure 7, produces the value of inertial acceleration that affected the measurements. Figure 11 shows the result of this subtraction operation.

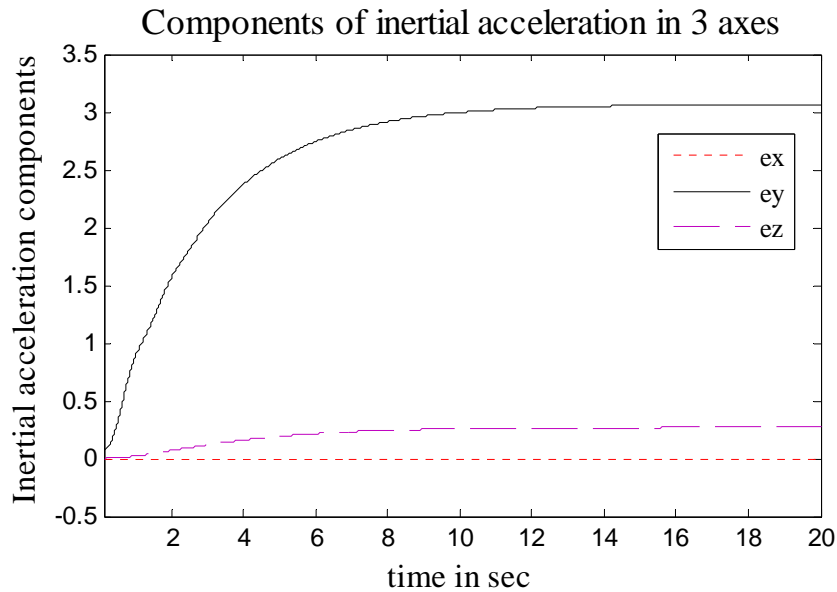


Figure 11. Inertial acceleration components e_x , e_y , e_z

It can be seen from the graph above that the y direction had an inertial acceleration component of nearly $3g$, z axis was affected by $0.25g$ and the x axis was unaffected by any extraneous disturbances.

In case the vehicle experiences disturbances such that all the twenty five Euler angle computation methods produce erroneous results and no majority vote is possible, then additional sensors like rate gyro could be employed when feasible. Rate gyro together with knowledge of vehicle flight dynamics and estimation algorithms like Kalman filter theory can help in estimating the vehicle's attitude. This can complement the Euler angle computation based on the accelerometer and magnetometer sensors.

5. JOY-STICK FORCE FEEDBACK SYSTEM

Most UAVs today are remotely controlled by human pilots through a joy-stick. Even if the UAV has an on-board stabilizing controller, the pilot still has to set the reference angles for the UAV. The range of angles for a safe flight is very limited especially when the UAV is taking off or landing. In such situations, there is very little room for error by the pilot. Any erroneous input by the pilot can cause the UAV to veer outside the safe flight envelope and crash.

The pilot generates the angle reference commands through moving/rotating the joy-stick. A force feedback on the joy-stick which prevents the user from giving erroneous inputs can go a long way in making the UAV pilot's job easier as well as make the UAV itself safer. Towards this goal, a prototype joy-stick assembly is constructed with the joy-stick attached to an actuator such as a DC motor. This prototype joy-stick assembly is used to generate the roll angle reference to the UAV. It demonstrates the force-feedback applied to the joy-stick. This prototype system hardware is described in the following.

5.1 Hardware description

In order to demonstrate the concept of force feedback on the joy-stick, a simple prototype is constructed. The schematic diagram of this prototype is shown in Figure 12.

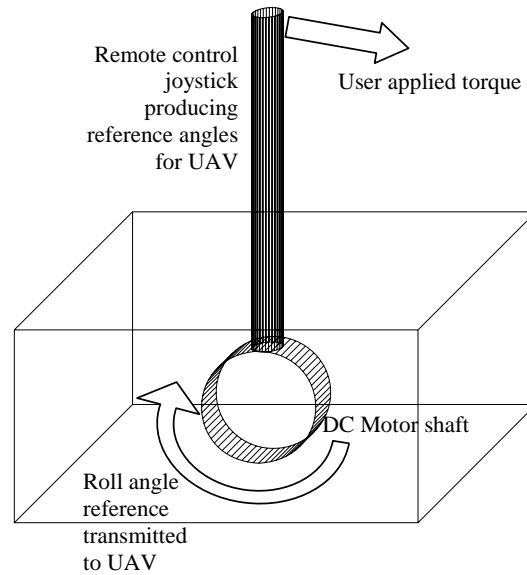


Figure 12. Prototype remote control joy-stick regulation system.

This system is constructed similar to a normal joy-stick but now the joy-stick base is attached to a DC motor shaft. This DC motor is also attached to an optical encoder. The joy-stick angle measured through the optical encoder is transmitted as the reference roll angle to the UAV. The UAV has its own feedback controller described in section 4.1 to maintain its stability and also to track the reference roll angle. But for every different flying condition like cruise, take-off or landing, there is a maximum roll angle within which the UAV remains stable and/or safe. Once the UAV roll angle exceeds the pre-defined safety limit, the DC motor attached to the joy-stick is controlled such that there is an increased resistance to any further joy-stick movement. Furthermore, the joy-stick will be rotated backward so as to produce reference commands which are within the safe region. This limiting mechanism on the joy-stick can help UAV pilots by providing a force feedback in addition to visual information. Once the UAV is within the safe flight envelope, the DC motor is de-activated so as to give full freedom to the pilot. This allows for an overall easy and less strenuous operation.

A feedback controller is designed to control the DC motor joy-stick assembly in order to achieve all these objectives. Measurements required for functioning of the controller are - the roll angle of the UAV and both the speed and position of the joy-stick. Roll angle can be obtained from the Euler angle computation method described in section 4.2. Speed and position of joy-stick are obtained using the optical encoders attached to the DC motor.

In order to develop a controller, it is necessary that the system be described mathematically. A mathematical model for the above prototype system is developed in the following.

5.2 Force Feedback Joy-Stick Dynamic Model

The prototype force feedback joy-stick system for the UAV consists of a joy-stick attached to the motor shaft of a DC motor. While DC motor forms the main component, the general mathematical description of the system has to also account for the user applied torque applied to the joy-stick. The dynamic model of the system is constructed as follows.

The main components in the force feedback assembly are the joy-stick and the DC motor. Apart from the voltage input V_m , this DC motor also has to accommodate the user applied torque τ_{app} applied through the joy-stick. Outputs of the system are angular position θ_m , angular speed $\dot{\theta}_m$ and current i_m . This system can be represented as:

$$G_m(s): \begin{cases} \dot{x}_m(t) = A_m x_m(t) + B_m u_m(t) \\ y_m(t) = C_m x_m(t) + D_m u_m(t) \end{cases} \quad (59)$$

$x_m(t)$, $u_m(t)$ and $y_m(t)$ are the state, control input, and output vectors, respectively.

$$x_m(t) = \begin{bmatrix} \theta_m \\ \dot{\theta}_m \\ i_m \end{bmatrix} \quad u_m(t) = \begin{bmatrix} V_m \\ \tau_{app} \end{bmatrix} \quad y_m(t) = \begin{bmatrix} \theta_m \\ \dot{\theta}_m \\ i_m \end{bmatrix} \quad (60)$$

The detailed mathematical description of the subsystem is shown in (61).

$$\frac{d}{dt} \begin{bmatrix} \theta_m \\ \dot{\theta}_m \\ i_m \end{bmatrix} = \begin{bmatrix} 0 & 1 & 0 \\ 0 & -b/J & K_b/J \\ 0 & -K_b/L & -R/L \end{bmatrix} \begin{bmatrix} \theta_m \\ \dot{\theta}_m \\ i_m \end{bmatrix} + \begin{bmatrix} 0 & 0 \\ 0 & 1/J \\ 1/L & 0 \end{bmatrix} \begin{bmatrix} V_m \\ \tau_{app} \end{bmatrix} \quad (61)$$

where, the numerical values of the motor parameters damping ratio b , moment of inertia J , torque/back-emf constant K_b , winding resistance R and inductance L are :

$$\begin{aligned} b &= 2.5e-7 \text{ N/m/s}, & J &= 2.7e-7 \text{ kg m}^2, \\ K_b &= 0.0177 \text{ Nm/A}, & R &= 21 \Omega, & L &= 900 \mu H. \end{aligned} \quad (62)$$

Substituting (62) into (61), numerical values of the master subsystem matrices are obtained as

$$\begin{aligned} A_m &= \begin{bmatrix} 0 & 1 & 0 \\ 0 & -0.9259 & 65556 \\ 0 & -19.667 & -23333 \end{bmatrix} & B_m &= \begin{bmatrix} 0 & 0 \\ 0 & 3.7e6 \\ 1.1e3 & 0 \end{bmatrix} \\ C_m &= \begin{bmatrix} 1 & 0 & 0 \\ 0 & 1 & 0 \\ 0 & 0 & 1 \end{bmatrix} & D_m &= \begin{bmatrix} 0 & 0 \\ 0 & 0 \\ 0 & 0 \end{bmatrix} \end{aligned} \quad (63)$$

One of the outputs of the system shown in (59) is the joy-stick angle θ_m . This acts as the reference roll angle to the UAV. The roll angle response of the UAV is feedback to the DC motor controller in order to control the joy-stick speed $\dot{\theta}_m$. A hybrid controller is designed to accomplish this task. The controller design and simulation of the overall closed loop system are given in the following chapter.

6. JOY-STICK FORCE FEEDBACK CONTROLLER DESIGN

6.1 Joy-Stick Speed Regulator – Hybrid Controller

In the control system block diagram shown in Figure 13, $G_m(s)$ is the plant or the joy-stick, DC motor assembly to be controlled. The dynamic model of this assembly is given in (59). $G_m(s)$ receives two inputs, one through the user applied torque τ_{app} and another - the control input voltage V_m . While user applied torque rotates the motor shaft through the joy-stick, the controller is designed to deliver an input voltage which alters the DC motor shaft angular speed and thereby affect the joy-stick movement.

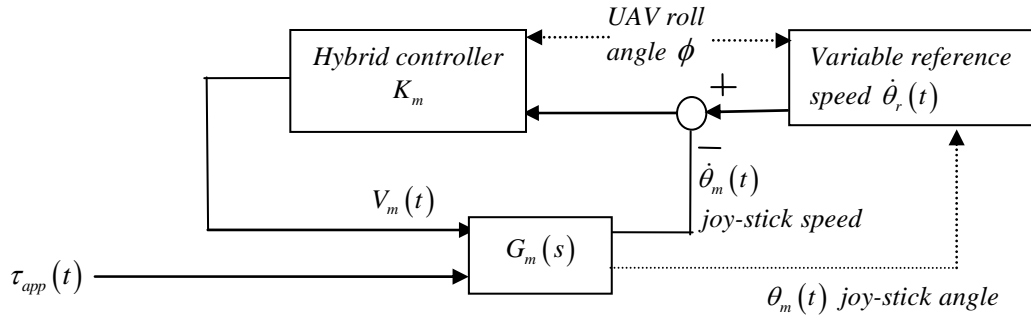


Figure 13. Joy-Stick angular speed regulation through variable feedback gain hybrid controller.

The MIMO plant - $G_m(s)$ is split up into two single input single output plants, one of which describes the transfer function relating V_m with $\dot{\theta}_m$ and the other describes the transfer function from τ_{app} to $\dot{\theta}_m$. The two SISO transfer functions are:

$$\begin{aligned}
 G_{mV}(s) &= \frac{\dot{\theta}_m(s)}{V_m(s)} = \frac{7.283e7}{s^2 + 2.33e4s + 1.311e6} \\
 G_{m\tau}(s) &= \frac{\dot{\theta}_m(s)}{\tau_{app}(s)} = \frac{3.704e6s + 8.642e10}{s^2 + 2.33e4s + 1.311e6}
 \end{aligned} \tag{64}$$

$G_{mV}(s)$ is of particular interest in the designing of the speed regulation controller. The objective is to design two controllers, one of which is a proportional and integral controller $K_1(s)$ for the transfer function $G_{mV}(s)$ such that stability of the system is maintained in addition to the task of regulating the speed. The second controller is just a zero or a no feedback.

The overall speed regulation controller K_m is a hybrid controller. It is activated or set to $K_1(s)$ when the UAV roll angle is over the maximum safe envelope roll angle. This causes a resistance or roll-back of the joy-stick. It is de-activated or set equal to 0 whenever its angle is within the safe envelope. This allows for a free movement of the joy-stick whenever the UAV is within the safe flight roll angle. The structure of the controller K_m is shown in (65).

$$\begin{aligned} \text{Activated} \quad K_m &\rightarrow K_1(s) = K_{pm} + \frac{K_{im}}{s} \\ \text{De-actiavted} \quad K_m &\rightarrow K_1(s) = 0 \end{aligned} \tag{65}$$

where,

K_{pm} is the proportional gain in the master motor controller

K_{im} is the integral gain

The reference speed of the joy-stick rotation is also altered depending on the measured UAV roll angle and the instantaneous joy-stick angle. If the joy-stick angle has exceeded the UAV safe roll angle, it needs to be brought back into the safe region. This is accomplished by selecting a negative reference speed. However, when the joy-stick angle is within the safe range, it can be held at the same place. This can be done by selecting

the reference joy-stick speed as zero. Flowchart in Figure 14 describes the switching strategy for the hybrid controller gains and reference speed.

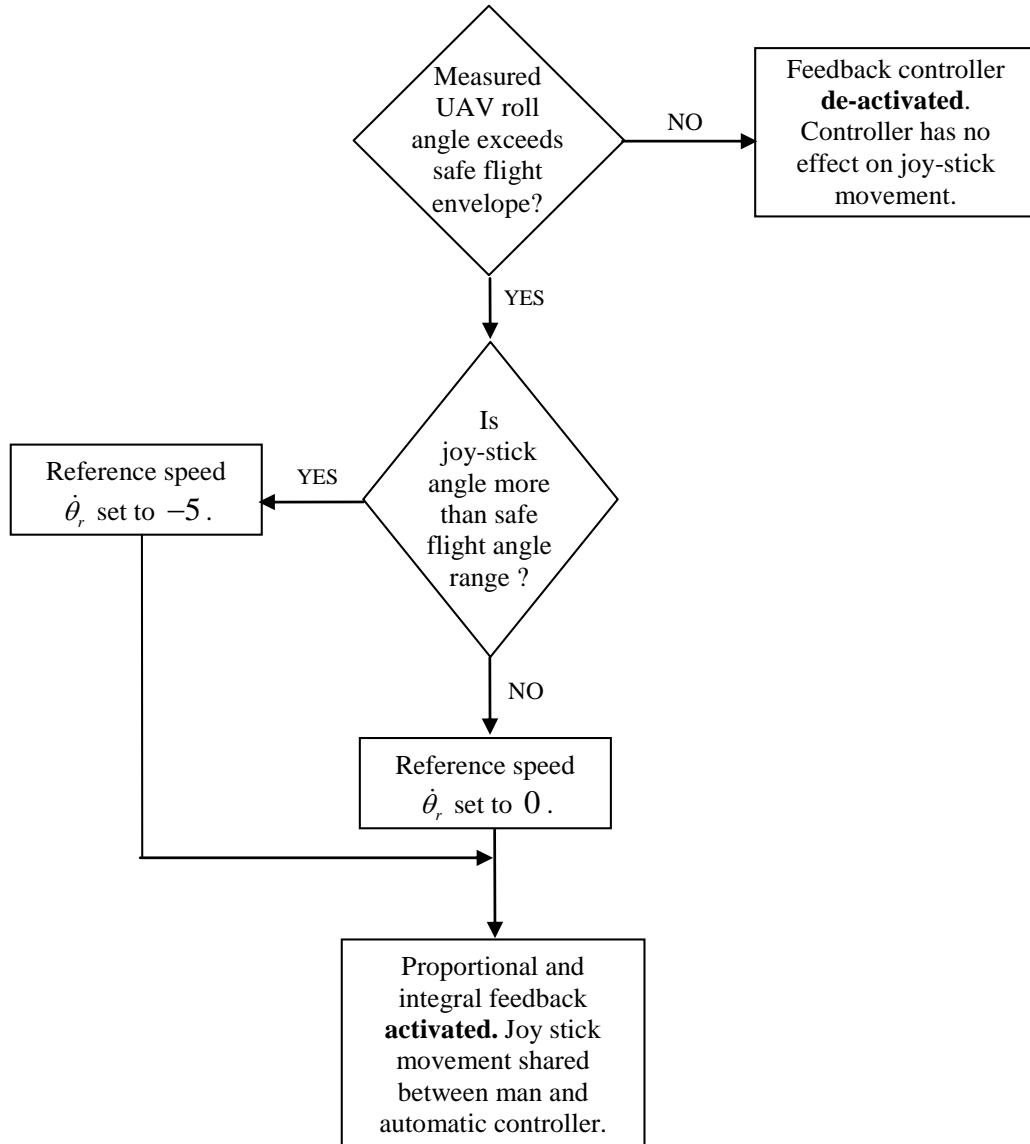


Figure 14. Master motor discrete hybrid controller switching strategy.

Numerical values of gains in the active PI controller were chosen based on stability analysis and experimental results. The most suitable proportional and integral gains respectively were found to be:

$$\begin{aligned} K_{pm} &= 0.06 \\ K_{im} &= 0.005 \end{aligned}$$

With these gains, the proportional and integral controller for the master motor speed regulation is seen to be:

$$\text{Activated } K_m \rightarrow K_1(s) = 0.06 + \frac{0.005}{s}$$

The loop transfer function relating the master motor speed $\dot{\theta}_m$ with the reference speed $\dot{\theta}_r$ can be given as :

$$K_1(s)G_{mv}(s) = \frac{4.37e6s + 3.642e5}{s^3 + 2.33e4s^2 + 1.311e6s} \quad (66)$$

The closed loop system with the active controller $K_1(s)$ is analyzed for stability through the Bode plot technique. Bode plot of the function in (66) is shown in Figure 15. This reveals that the gain and phase margin of the system is ∞ and 107° respectively.

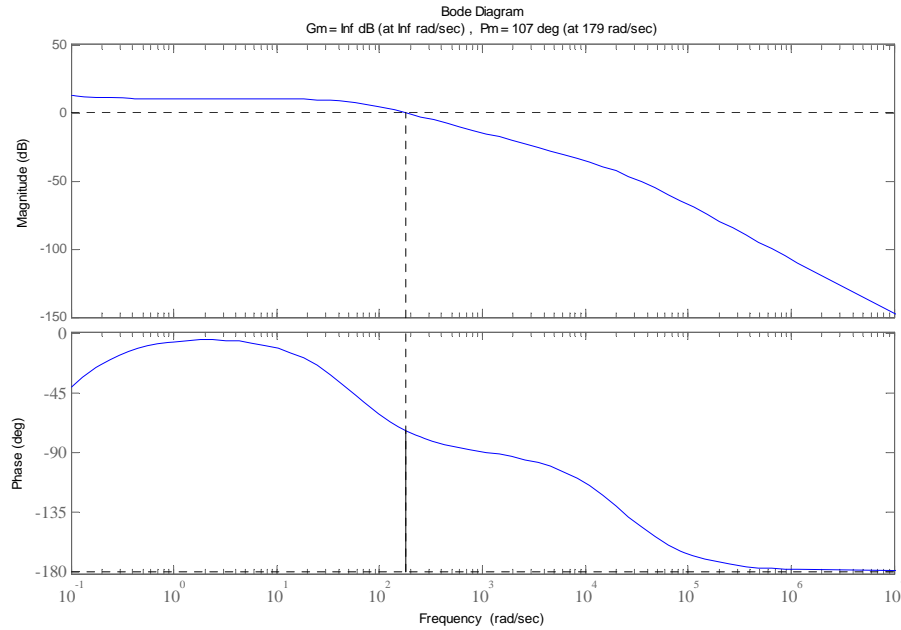


Figure 15. Bode plot of DC motor with PI controller.

Thus it can be concluded that the closed loop system with the activated speed controller is stable for any bounded input. The de-activated controller has zero as its gains and the plant itself is stable thus the closed loop plant with the de-activated controller is also stable. This overall system with the hybrid controller can therefore be considered stable.

6.2 UAV stabilization and tracking controller

The stabilization and tracking regulation controller for the UAV was developed in Section 4.1. The reference signal was considered to be a step signal. But when the pilot gives reference roll angle commands through a joy-stick, it resembles a ramp signal rather than a step. This new reference signal can be represented as:

$$\dot{r}(t) = Zr(t) \quad \text{with} \quad Z = \begin{bmatrix} 0 & 1 \\ 0 & 0 \end{bmatrix} \quad (67)$$

The regulator matrices U and W corresponding to the reference signal $r(t)$ shown in (67) are computed such that the equations (51) and (52) are satisfied. These matrices are used in construction of the new stabilization and tracking controller - K_n . K_n has the structure as shown in Figure 6.

6.3 Overall Closed Loop System & Computer Simulation

The overall closed system is formed by combining the joy-stick assembly with the UAV. The closed loop system is shown in Figure 16. This overall system is simulated. The reference roll angle for the UAV is produced by the joy-stick, while the reference speed for the joy-stick depends on the actual roll angle of the UAV.

In this simulation the limiting roll angle is chosen as 5° . Initially the UAV is assumed to be in level flight with roll angle nearly 0° . The joy-stick angle is also assumed to be 0° at the beginning of the simulation. The pilot intends to make the UAV reach the maximum allowed roll angle and stay close to that state. With this intention he applies a torque τ_{app} [33] on the joy-stick in the form shown in the graph of Figure 17. After 12 sec, he momentarily decreases the torque to zero and then applies a small negative torque at time 14.5 sec. At time 17 sec there is an accidental high torque applied to the joy-stick. The response of the joy-stick and the UAV to this input by the user is shown in Figure 18.

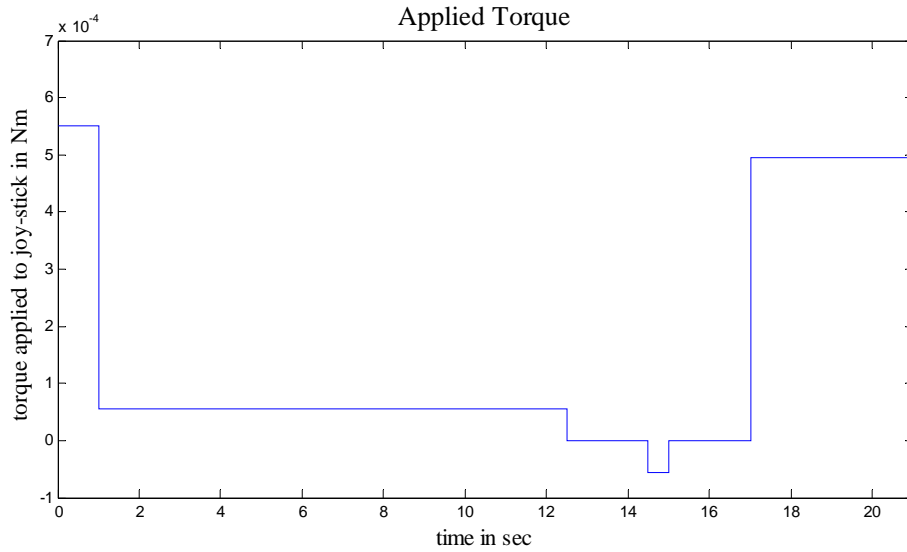


Figure 17. User applied input torque to joy-stick.

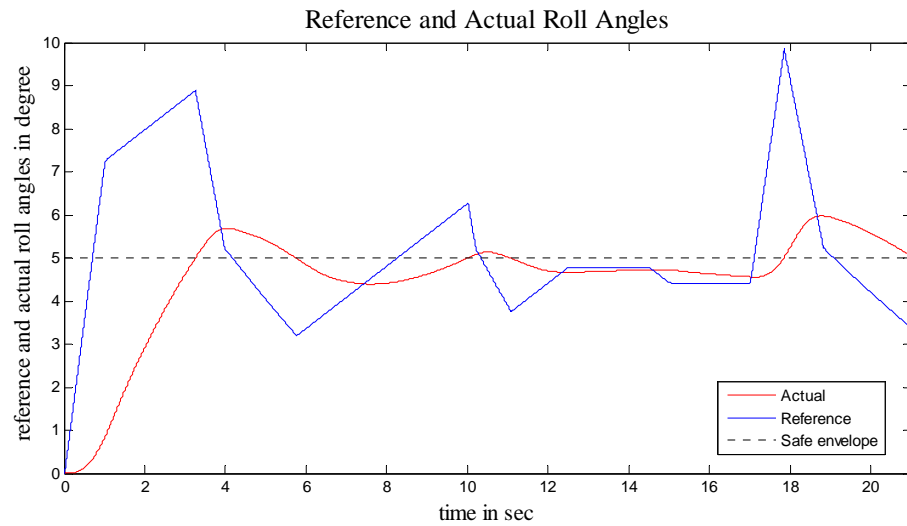


Figure 18. Reference roll angle applied by joy-stick angle and the UAV response.

For the UAV roll angle to reach 5° , the joy-stick has to be held exactly at an angle of 5° . But the user inputs on any joy-stick are not accurate. In this case it is seen that initially the user applies a large torque and the joy-stick angle or the reference command angle is overshoot. Later the user reduces his torque level. But by now the joy stick angle or the reference has already reached almost 9° . The UAV tracks the given reference roll angle

though it is very sluggish. It is seen that as soon as the UAV roll angle ϕ or the actual angle reaches 5° , the joy-stick is rotated backward despite an unchanged user applied torque. Once the UAV angle goes below 5° again, the PI controller is de-activated allowing free movement for the pilot. The control actions done by the PI controller can be understood by observing the DC motor control input voltage graph shown in Figure 19. It is seen that a negative voltage is applied every time the measured UAV angle exceeds 5° . This voltage either opposes or resists the joy-stick movement. But whenever the UAV is within safe flight envelope, there is no voltage applied to oppose any movement of the joy-stick. This is seen from time 11 sec to 18 sec in Figure 19. All through this time, the UAV roll angle was maintained within 5° and the control voltage on the joy-stick is seen to be zero. At time 17 sec, a large erroneous torque is applied by the user/pilot. This increases the joy-stick reference angle to nearly 10° . But as soon as the UAV roll angle or actual angle exceeds the safe envelope, the joy-stick is rotated backward. This demonstrates that this system helps in preventing accidental wrong inputs to the UAV.

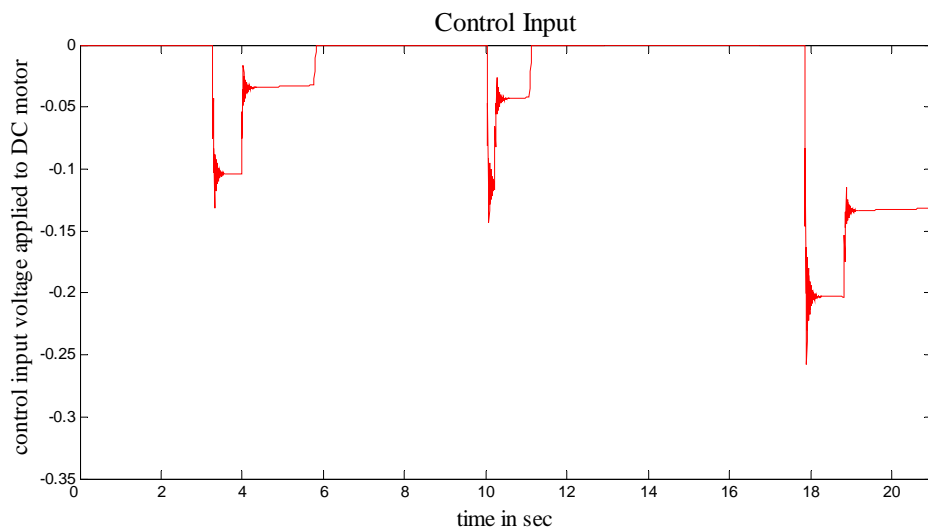


Figure 19. DC motor control input voltage.

This simulation demonstrated that the force feedback on the joy-stick helped maintain the roll angle of the UAV around the safe flight envelope despite user applied torque levels forcing the joy-stick to larger angles. Even an accidental high torque was handled well by the system. The UAV was always maintained within 20% of the pre-defined limiting angle.

7. CONCLUSION

A new type of redundancy was introduced in this document where a minimal increase in hardware and increased computation resulted in a new type of redundancy called as diversified redundancy. This helped improve fault tolerance of the available sensors. Twenty five different methods of Euler angle computation were introduced where almost all of them utilized different subsets of sensor measurements from among the three accelerometer and three magnetometers. The ability to compute the same Euler angles in multiple ways using different subset of sensor data provides diversified redundancy that improved the performance and reliability of the sensing system. Even in the face of faults on certain sets of sensors, Euler angles could be accurately determined. A bank-to-turn maneuver example of the NASA GTM UAV has demonstrated the ability of the proposed approach to identify the faulty sensors and also to find the correct Euler angles despite the interference on 2 of the 3 accelerometer measurements. Computing the value of the disturbance field was also demonstrated through the same example.

Since the proposed equations all involve inverse trigonometric functions, they lead to the numerical issues: quadrant selection and numerical instability near singularity points. The quadrant selection issue has been resolved under the assumption that the initial Euler angles are known and the sampling period is small enough that the angles do not change abruptly within one sampling period. Some Euler angle computation formulas are found to be more reliable than others near singularity as discussed in the paper. This before hand knowledge of weaknesses of each method can be accounted for in the majority voting algorithm. Thus the numerical instability issue was taken care of effectively and also used to our advantage.

When the accelerometers and magnetometers are influenced by extraneous field to a point where all the twenty-five computation formulas are unable to yield correct results, and no majority is available, additional sensors like 3 axis MEMS rate gyro along with vehicle flight dynamic model and observers like Kalman filters could help in indirect estimation of the attitude.

A modified joy-stick assembly was designed such that its movement was affected by both pilot applied torque and the actuator torque. In this proposed approach, the human is allowed freedom to maneuver the vehicle but this freedom is only within the safe flight envelope. Once it is determined that the UAV is outside the safe envelope, machine takes action and provides a force feedback such that it stops the pilot and thereby joy-stick from giving further erroneous inputs. This goal was achieved by designing a hybrid controller to control the actuator. Designing such an actuator controlled limit on the joy-stick allowed for flexibility. Depending on the flight condition this limit/safe envelope could be adjusted to allow for maximum maneuverability and thus maximum possible performance. This flexibility in setting the limit sets it apart from a mechanical joy-stick limiter where such a limit could have compromised maneuverability and therefore the performance of the UAV.

The resulting overall closed loop system was simulated. The performance of the system was such that it disallowed the UAV from exceeding the limiting roll angle by more than 20%. This control was effective despite an almost constant pilot applied torque on the joy-stick and an accidental large torque applied again by the pilot towards the end of the experiment. As long as the UAV was within the limiting roll angle, the actuator was seen

to apply no torque to oppose pilot applied torque thus allowing free movement and an easy, less strenuous operation.

List of References

- [1] James R.Wertz (ed.) et. al., “*Spacecraft attitude determination and Control*”, D. Reidel publishing company, 1978.

- [2] F. Landis Markley and Daniele Mortari “*How To Estimate Attitude From Vector Observations*”, AAS/AIAA Astrodynamics Specialist Conference, Girdwood, Alaska August 16-19, 1999, AAS 99-427.

- [3] Malcolm D. Shuster¹ and F. Landis Markley, “*Generalization of the Euler Angles*”, The Journal of the astronautical Sciences, Vol. 51, No. 2, April-June 2003, pp 123-132.

- [4] R. Pio, "Euler angle transformations," *IEEE Transactions on Automatic Control*, vol. 11, pp. 707-715, October 1966.

- [5] Lidai Wang; Shenshu Xiong; Zhaoying Zhou; Qian Wei; Jinhui Lan, "Constrained Filtering Method for MAV Attitude Determination," Instrumentation and Measurement Technology Conference, 2005. IMTC 2005. Proceedings of the IEEE , vol.2, no.pp. 1480- 1483, 16-19 May 2005.

- [6] Castellanos, J.F.G.; Lesecq, S.; Marchand, N.; Delamare, J., "A low-cost air data attitude heading reference system for the tourism airplane applications," *Sensors*, 2005 *IEEE* , vol., no., pp. 4 pp.-, 30 Oct.-3 Nov. 2005.

- [7] R. J. Patton, "Fault-tolerant Control: The 1997 situation", *IFAC Fault Detection, Supervision and Safety of Technical Processes*, Kingston upon Hull, UK, 1997, pp.1029-1051.

- [8] Suyama, K. “Fault detection of redundant sensors and used in reliable sampled-data control systems”. Proceedings of the 37th IEEE Conference on Decision and Control 1998, Vol.1, Iss., 1998 Pages 1161-1164 vol.1

[9] MEMSIC, “*Application Note: Accelerometer Fundamentals, #AN-00MX-001*”, 2007. [Online] <http://www.memsic.com/data/pdfs/an-00mx-001.pdf>, [Accessed – April 20, 2009].

[10] Girija Gopalaratnam, Cristoph Zorn and Andreas Koch, “*Multi Sensor Data fusion for Sensor Failure Detection and Health Monitoring*” AIAA Guidance, Navigation and Control Conference and Exhibit, 15-18 August 2005, San Francisco, California, AIAA 2005-5843.

[11] C. Jagadish and B. C. Chang, “*Diversified redundancy in the measurement of Euler angles using accelerometers and magnetometers*,” in *The 46th IEEE Conference on Decision and Control*, New Orleans, 2007, pp. 2669-2674.

[12] Grewal, M.S. and M. Shiva. *Application of Kalman filtering to gyroless attitude determination and control system for environmental satellites*. Decision and Control, 1995., Proceedings of the 34th IEEE Conference on, Vol.2, Iss., 13-15 Dec-1995 Pages:1544-1552 vol.2.

[13] Chirag Jagadish, Bor-Chin Chang, “*Fault Tolerant attitude computation for unmanned aerial vehicles*”, *Transactions of the Institute of Measurement & Control*, special issue on *Measurement & Estimation for Unmanned Navigation* (in-press).

[14] Hou, Y.; Gao, Z.; Jiang, F.; Boulter, B.T., “*Active disturbance rejection control for web tension regulation*,” *Decision and Control*, 2001. Proceedings of the 40th IEEE Conference on , vol.5, no., pp.4974-4979 vol.5, 2001.

[15] Hu, C.; Meng, M.; Liu, P.X.; Wang, X., “*Optimal digital control system design for winding shaping process of automobile belt*,” *Electrical and Computer Engineering*, 2003. IEEE CCECE 2003. Canadian Conference on , vol.3, no., pp. 1763-1766 vol.3, 4-7 May 2003.

[16] Guo Shuai; He Yongyi; Fang Minglun; Lu Lixin, “*Design of a fuzzy pre-compensator PID tension controller for fabric based on DSP*,” *Control, Automation, Robotics and Vision Conference*, 2004. ICARCV 2004 8th , vol.3, no., pp. 1895-1900 Vol. 3, 6-9 Dec. 2004

[17] Stan, E.; McNames, J.; Kohles, S.S.; Biber, C.; Biberic, N.; Leech, N.; Mangan, R.W.; McKinney, T.J.; Surdu, M.; Goldstein, B., "Mechanical vasoconstriction for a cerebral myogenic autoregulatory model," *Engineering in Medicine and Biology Society*, 2004. IEMBS '04. 26th Annual International Conference of the IEEE , vol.1, no., pp.883-886, 1-5 Sept. 2004

[18] F. Wang; E. Burdet; R. Vuillemin; H. Bleuler, "Knot-tying with Visual and Force Feedback for VR Laparoscopic Training," *Engineering in Medicine and Biology Society*, 2005. *IEEE-EMBS 2005. 27th Annual International Conference of the* , vol., no., pp.5778-5781, 2005

[19] Byunghoon Bae, Taeoh Koo, Kyihwan Park and Yongdae Kim, "Design and Control of a Two Degree of Freedom Haptic Device for the Application of PC Video Games," *Proceedings of the 2001 IEEE/RSJ International Conference on Intelligent Robots and Systems*, Maui, Hawaii, USA Oct. 29 – Nov. 03, 2001, pp. 1738 – 1743.

[20] Fattouh, A.; Sahnoun, M.; Bourhis, G., "Force feedback joystick control of a powered wheelchair: preliminary study," *Systems, Man and Cybernetics, 2004 IEEE International Conference on* , vol.3, no., pp. 2640-2645 vol.3, 10-13 Oct. 2004

[21] R. A. Cooper, D. M. Spaeth, D. K. Jones, M. L., "Comparison of virtual and real powered wheelchair driving using a position sensing joystick and an isometric joystick", *Medical Engineering and Physics*, vol. 24, pp. 703-708, 2002

[22] David M. Brienza; Jennifer Angelo, "A force feedback joystick and control algorithm for wheelchair obstacle avoidance", *Disability & Rehabilitation*, 1464-5165, Volume 18, Issue 3, 1996, Pages 123 – 129

[23] Texas Instruments, "Texas Instruments DSP Microprocessor TMS320F2812 Data Manual", Tech. Rep. SPRS1740, April 2001 – Revised July 2007. [Online].

[24] Texas Instrumntents, *TMS320F28x DSP Event Manager Reference Guide*, Literature Number: SPRU065B, Nov. 2003.

[25] H. Sira-Ramirez, "A Geometric Approach to Pulse-Width Modulated Control in Nonlinear Dynamical Systems," *IEEE Trans. On Automatic Control*, Vol. 34, 1989.

[26] T.A. Sakharuk, B. Lehman, A.M. Stankovic, and G. Tadmor, "Effects of Finite Switching Frequency and Delay on PWM Controlled Systems," *IEEE Trans. On Circuits and Systems—I: Fundamental Theory and Applications*, Vol. 47, pp. 555 – 567, 2000.

[27] BLACK, H. D. "A Passive System for Determining the Attitude of a Satellite," *AIAA Journal*, Vol. 2, July 1964, pp. 1350–1351.

[28] KEAT, J. "Analysis of Least Squares Attitude Determination Routine DOAOP," Computer Sciences Corporation, CSC/TM–77/6034, February 1977.

[29] WAHBA, G. "Problem 65-1: A Least Squares Estimate of Spacecraft Attitude," *SIAM Review*, Vol. 7, No. 3, July 1965, p. 409.

[30] Malcolm D.Shuster. "The Quest for Better Attitudes", *The Journal of the Astronautical Sciences*, Vol. 54, Nos. 3 & 4, pp.657-683, July-December 2006.

[31] Honeywell, "*Application Note 213: "Set/Reset Function for the Magnetic Sensors"*", Honeywell Sensor Products, Solid State Electronics Center, 2002, [Online] <http://www.ssec.honeywell.com/magnetic/datasheets/an213.pdf>, [Accessed – April 20, 2009].

[32] National Geophysical Data Center (NGDC), Geomagnetism, 2007. [Online] <http://www.ngdc.noaa.gov/geomag/>, [Accessed – April 20, 2009].

[33] A.D Swain, G.C. Shelton, L.V. Rigby, "Maximum torque for small knobs operated without gloves", *Ergonomics*, Volume 13, Issue 2, March 1970, pages 201-208.

[34] Analog Devices, *Low-cost, Single supply, Differential amplifier*, Data Sheet Rev D, 01//2003.

APPENDIX A

Notation

x^T	Transpose of vector x
A^T	transpose of matrix A
\dot{x}	Time derivative of x
$c\theta$	Cosine of θ
$s\theta$	Sine of θ
$E[X]$	Expected value of X

Abbreviations

UAV	Unmanned aerial vehicle
DSP	Digital signal processor
TI	Texas instruments
DC	Direct current
MEMS	Micro electro-mechanical systems
AMR	Anisotropic Magneto Resistive
YPR	Yaw Pitch Roll rotation sequence
YRP	Yaw Roll Pitch rotation sequence
PWM	Pulse width modulation
ADC	Analog to digital conversion/converter
QEP	Quadrature encoder pulse
CPU	Central processing unit

SISO	Single input single output
MIMO	Multi input multi output
CCS	Code composer studio

Symbols

ϕ, θ, ψ - Roll, Pitch and Yaw angles corresponding to aerospace sequence rotation

g_x, g_y, g_z - Gravity measured in 3 mutually perpendicular directions x, y and z .

m_x, m_y, m_z - Earth magnetic field measured in x, y and z directions.

$\hat{u}, \hat{v}, \hat{w}$ - Measured reference vectors.

u_1, u_2, u_3 - The 3 components of \hat{u} .

b_i - 3 dimensional vector measurement used in Q method

r_i - 3 dimensional reference vector used in Q method

a_i - Weighting for each individual measurement vector

Q_u - Unit quaternion

Q_{opt} - Optimal quaternion

$[q, q_4]$ - Components of the quaternion

λ_{\max} - Maximal eigenvalue which minimizes Wahba's loss function

K_e - Eigenvector corresponding to maximal eigenvalue

$[x, y, z]$ - Vector of measurement at initial angular position

$[x', y', z']$ - Vector of measurement after rotation about first axis

$[x'', y'', z'']$ - Vector of measurement after rotation about second axis

$[u \ v \ w]$ - Vector of measurement after rotation about last/third axis

α - Inclination angle of earth magnetic field

$[i_x \ i_y \ i_z]$ - Any initial measurement vector

$[o_x \ o_y \ o_z]$ - Final vector corresponding to the initial vector

$[\alpha] \ [\beta]$ - Rotation matrices

$[\theta_1, \phi_1, \psi_1]$ - Rotation angles corresponding to RPY (Roll Pitch Yaw) rotation sequence

$x(t), u(t), y(t)$ - state, control input, and output vectors of UAV

β - Side slip angle of UAV

p - Roll rate of UAV

q - Yaw rate of UAV

ϕ - Roll angle of UAV

δ_a, δ_r - Aileron and rudder angle

$w_d(t), v(t)$ - Disturbances and noises affecting the UAV

$r(t)$ - Reference roll angle command input to UAV

$A, B_2, B_1, C_{1u}, C_2, D_{11u}, D_{12d}, D_{21}, D_{22}$ - System matrices of dynamic model describing UAV

X - Positive semi-definite stabilizing solution of the algebraic Riccati equation

F, U, W - Controller matrices for UAV

K - Controller for UAV

e_x, e_y, e_z - Inertial acceleration components

$G_m(s)$ - Plant or the joy-stick, DC motor assembly to be controlled

τ_{app} - User applied torque input to joy-stick assembly

V_m - Control input voltage applied by joy-stick assembly feedback controller

$\theta_m, \dot{\theta}_m, i_m$ - Angular position, angular speed and current in DC motor connected to joy-stick

$x_m(t), u_m(t), y_m(t)$ - State, Control input, and Output vectors of joy-stick assembly dynamic model

b - damping ratio of DC motor

J moment of inertia of DC motor

K_b torque/back-emf constant of DC motor

R winding resistance of DC motor

L inductance of DC motor

A_m, B_m, C_m, D_m - Matrices of system dynamic model of joy-stick assembly

$G_{mV}(s)$ - Transfer function relating control input voltage to angular speed of joy-stick assembly

K_m - Hybrid controller designed to control the joy-stick assembly

$K_I(s)$ - Hybrid controller activated or PI controller

K_{pm}, K_{im} - Proportional and integral gains of the master motor controller

VITA

CHIRAG JAGADISH

EDUCATION

Doctor of Philosophy, Mechanical Engineering and Mechanics, Drexel University, June 2009.

Master of Science, Mechanical Engineering and Mechanics, Drexel University, June 2007.

Bachelor of Engineering, Electronics and Communication Engineering, Visveswaraiah Technological University, Karnataka, India, March 2002.

RESEARCH INTERESTS

Sensors, Control system & implementation, Microprocessors & Digital Signal Processors, Robotics, Automation.

RESEARCH EXPERIENCE

Graduate Research Assistant, December 2004 – June 2009

System and Control Labs, Mechanical Engineering and Mechanics Department, Drexel University Philadelphia PA USA.

TEACHING EXPERIENCE

Teaching Assistant, December 2004 – June 2009

Mechanical Engineering and Mechanics Department, Drexel University Philadelphia PA USA.

PUBLICATIONS

C. Jagadish and B. C. Chang, "*Diversified redundancy in the measurement of Euler angles using accelerometers and magnetometers*," in *Proceedings of the 46th IEEE Conference on Decision and Control*, New Orleans, 2007, pp. 2669-2674.

Chirag Jagadish, Bor-Chin Chang, "*Fault Tolerant attitude computation for unmanned aerial vehicles*", *Transactions of the Institute of Measurement & Control*, special issue on *Measurement & Estimation for Unmanned Navigation* (in-press).

